Atmos. Chem. Phys., 18, 9121–9145, 2018
https://doi.org/10.5194/acp-18-9121-2018


Atmospheric Chemistry and Physics
Open Access
EGU

# The Green Ocean: precipitation insights from the GoAmazon2014/5 experiment

**Die Wang[1], Scott E. Giangrande[1], Mary Jane Bartholomew[1], Joseph Hardin[2], Zhe Feng[2], Ryan Thalman[3], and Luiz A. T. Machado[4]**

[1]Environmental and Climate Sciences Department, Brookhaven National Laboratory, Upton, NY, USA
[2]Pacific Northwest National Laboratory, Richland, WA, USA
[3]Department of Chemistry, Snow College, Richfield, UT, USA
[4]National Institute for Space Research, São José dos Campos, Brazil

**Correspondence:** Die Wang (diewang@bnl.gov)

Received: 30 January 2018 – Discussion started: 7 February 2018
Revised: 15 June 2018 – Accepted: 18 June 2018 – Published: 29 June 2018

**Abstract.** This study summarizes the precipitation properties collected during the GoAmazon2014/5 campaign near Manaus in central Amazonia, Brazil. Precipitation breakdowns, summary radar rainfall relationships and self-consistency concepts from a coupled disdrometer and radar wind profiler measurements are presented. The properties of Amazon cumulus and associated stratiform precipitation are discussed, including segregations according to seasonal (wet or dry regime) variability, cloud echo-top height and possible aerosol influences on the apparent oceanic characteristics of the precipitation drop size distributions. Overall, we observe that the Amazon precipitation straddles behaviors found during previous U.S. Department of Energy Atmospheric Radiation Measurement (ARM) program tropical deployments, with distributions favoring higher concentrations of smaller drops than ARM continental examples. Oceanic-type precipitation characteristics are predominantly observed during the Amazon wet seasons. An exploration of the controls on wet season precipitation properties reveals that wind direction, compared with other standard radiosonde thermodynamic parameters or aerosol count/regime classifications performed at the ARM site, provides a good indicator for those wet season Amazon events having an oceanic character for their precipitation drop size distributions.

## 1 Introduction

Global climate models (GCMs) continuously improve to overcome deficiencies in climate predictions associated with cloud and precipitation processes (e.g., Klein and Genio, 2006; Del Genio, 2012). Following suit, observational studies serve to inform GCM and cloud-resolving model (CRM) activities by providing the physical understanding for more diverse, climatically significant global cloud conditions and their associated feedbacks. Cumulus to deeper convective clouds are associated with high-impact weather events and act as the engine of global circulation. Subsequently, model treatments of convection have a profound impact on weather and climate simulations. For practical reasons, the evaluation of cumulus treatments has often stressed comparisons against larger-scale, longer-term precipitation properties, for example, accumulated rainfall products from ground or spaceborne instruments (e.g., Hou et al., 2014). Thus, a traditional observational approach in support of convective modeling has been to document global precipitation variability and improve basic rainfall retrievals. Nevertheless, improving model capabilities introduces new challenges that motivate multi-scale, multi-sensor observations to better constrain cloud microphysics and dynamics closer to the process levels future GCMs attempt to represent (e.g., Mather and Voyles, 2013; Donner et al., 2016).

Recently, the Observations and Modeling of the Green Ocean Amazon (GoAmazon2014/5) experiment was motivated by demands to gain a better understanding of aerosol, cloud and precipitation interactions on climate and global circulation (Martin et al., 2016, 2017). One source of un-

certainty when developing useful precipitation retrievals for model development is the shortage of long-term surface gauge and disdrometer observations within tropical regions. Although radar rainfall estimation and its uncertainty for tropical applications is of primary interest, basic radar preprocessing, calibration and dual-polarization radar data quality are also improved with extended surface precipitation records in diverse environments. Establishing boundaries for tropical precipitation expectations and radar data quality concepts (self-consistency methods; e.g., Scarchilli et al., 1996) provides an immediate benefit when interpreting remote radar deployment datasets including those from the Atmospheric Radiation Measurement (ARM; Ackerman and Stokes, 2003) mobile facility (AMF; Miller et al., 2016) during GoAmazon2014/5. Specifically, the Amazon basin offers a unique tropical perspective on the variability in precipitation, as it receives copious precipitation across diverse cloud conditions, including wet and dry seasonal variability interconnected to large-scale shifts in the thermodynamic forcing and coupled local cloud-scale feedbacks (e.g., Machado et al., 2004; Cifelli et al., 2004; Li and Fu, 2004; Misra, 2008).

Although improving hydrological retrievals is of a practical significance, an interesting outcome from previous Amazon studies is the labeling of the Amazon as the "Green Ocean". This Green Ocean terminology is rooted in studies such as Roberts et al. (2001) wherein low cloud condensation nuclei (CCN) concentrations and high CCN-to-condensation nuclei (CN) ratios over the Amazon resembled marine environments, distinct from previous continental expectations. However, this terminology is often extended to include the unique regional characteristics observed from Amazon convection that span oceanic to continental cloud extremes in key attributes such as updraft intensities and propensity for electrification. Specific to convection, Amazon clouds may initiate under these clean (or lower) CCN conditions or over a pristine forest, but they may also experience a range of thermodynamical and aerosol forcing influences that promote changes in cloud properties including electrification, cloud droplet size distribution and precipitation changes, or enhanced updraft intensity (e.g., Williams et al., 2002; Cecchini et al., 2016; Giangrande et al., 2016b, 2017). As described by Williams et al. (2002), the prevalence of maritime convective cloud regimes over a large continent are possibly still underappreciated in the convective cloud spectrum and its intensity, especially given the propensity to identify deeper convection over the Amazon having electrification, arguing continental convective characteristics.

To understand the diversity of convective clouds as well as to constrain upcoming convective modeling activities from GoAmazon2014/5, it is informative to explore Amazon cumulus characteristics over this extended dataset. One motivation for this study is to identify conditions under which precipitation sampled in the Amazon basin adheres more to oceanic, maritime and continental characteristics (e.g., Tokay and Short, 1996). Previous ARM Tropical Western Pacific (TWP; e.g., Long et al., 2016) precipitation studies have helped identify practical thresholds and composite behaviors for convection, as well as the strengths/deficiencies for more practical convective cloud regime segregations under various larger-scale monsoonal and more oceanic cloud environments (e.g., Bringi et al., 2003; Giangrande et al., 2014a; Thompson et al., 2015). While it is important to view these Amazon datasets and cloud or larger-scale regime shifts in the context of global disdrometer observations (e.g., Dolan et al., 2018), it is also useful to determine whether common remote-sensing platforms (e.g., dual-polarization quantities as from X-band to S-band radars) are sensitive to these differences.

This study summarizes the precipitation properties collected by the ARM AMF during GoAmazon2014/5 at the "T3" site located approximately 70 km to the west of Manaus in central Amazonia, Brazil (3°12′46.70″ S, 60°35′53.0″ W). The location samples both the local pristine atmosphere and the possible effects of the Manaus, Brazil, pollution plume. The T3 site was equipped to capture continuous convective cloud and precipitation column characteristics from a reconfigured radar wind profiler coupled with a ground disdrometer. Section 2 describes the instrumentation, methods and sources for uncertainty in results presented by this study. Precipitation comparisons from the disdrometer using traditional drop size distribution (DSD) parameters and dual-polarization quantities are located in Sect. 3. Sections 4 and 5 discuss the properties of the Amazon cumulus convective and associated stratiform precipitation, including segregations according to seasonal (wet or dry regime) variability, cloud height and possible aerosol influences. A summary of the key findings and discussions about the Amazon as a Green Ocean are provided in the final section.

## 2 Dataset and methodology

### 2.1 ARM T3 precipitation and radar wind profiler dataset and processing

Precipitation observations are obtained from two primary instruments, a second-generation particle size velocity (PARSIVEL) disdrometer (e.g., Löffler-Mang and Joss, 2000; Tokay et al., 2014; Bartholomew, 2014) and a reconfigured 1290 MHz radar wind profiler (RWP; Giangrande et al., 2013, 2016b; Coulter et al., 2009). The collocated sensors capture surface DSDs, as well as simultaneous profiles for the vertical velocity and reflectivity factor estimates through the depth of Amazon clouds. These instruments operated concurrently from September 2014 through December 2015, a period that captured one wet season (herein, the 5 months defined as December through April) and one dry season (herein, periods from June through September). Additional information on the AMF deployment, including de-

tails on the larger-scale thermodynamic sampling throughout the campaign and appropriateness for wet or dry regime separations, is found in the GoAmazon2014/5 overview by Giangrande et al. (2017).

PARSIVEL measurements such as estimated DSD parameters and additional derived radar quantities are determined using 5 min aggregation windows. This sampling reduces noisiness found in 1 min DSD quantity retrievals, which is reduced further by selecting 5 min DSDs having $R > 0.5\,\mathrm{mm\,h^{-1}}$ and total drops > 100. In total, 3852 5 min DSDs were collected during the GoAmazon2014/5 campaign, with 3087 associated with the collocated RWP observations. The total precipitation associated with the full set of DSD observations is 2597 mm, with 2511 mm associated with collocated RWP observations. Approximately 1500 mm were associated with convective precipitation (RWP classifications to be discussed in later sections). Processing for the disdrometer was performed using the open-source PyDSD code (Hardin, 2014), with standard corrections (e.g., Tokay et al., 2013, 2014). Estimated quantities include the rainfall rate $R$ ($\mathrm{mm\,h^{-1}}$), rain water content (LWC, $\mathrm{g\,m^{-3}}$), measured median volume drop size $D_0$ (mm), and the mass-weighted mean diameter $D_\mathrm{m}$ (mm). Processing also includes additional parameters of a gamma-fit DSD assumed to be of the form $N(D) = N_0 D^\mu \exp(-\Lambda D)$, having volume diameter $D$ (mm) equivalent to number concentration $N_0$ ($\mathrm{mm^{-1}\,m^{-3}}$), shape parameter $\mu$ and slope parameter $\Lambda$ ($\mathrm{mm^{-1}}$) calculated following a method of higher moments (second, fourth and sixth moments; e.g., Cao and Zhang, 2009).

Additional calculations for a normalized DSD intercept parameter $N_\mathrm{w}$ have been adapted following Testud et al. (2001). These are required to investigate a DSD-based convective–stratiform partitioning scheme based on disdrometer observations (e.g., Bringi et al., 2002, 2003, 2009). Dual-polarization radar quantities including the radar reflectivity factor $Z$ (dBZ), differential reflectivity factor $Z_\mathrm{DR}$ (dB), specific differential phase $K_\mathrm{DP}$ ($\mathrm{deg\,km^{-1}}$) and specific attenuation $A$ ($\mathrm{dB\,km^{-1}}$, horizontal polarization) are estimated for liquid media at 20 °C using a T-matrix approach (e.g., Mishchenko et al., 1996). These estimates assume nonspherical drop shapes according to the relationship in Thurai et al. (2007) and standard drop canting assumptions for S-band (10 cm), C-band (5.45 cm) and X-band (3.16 cm) wavelengths.

RWP measurement details have been summarized by several recent studies, with precipitation datasets available at high spatiotemporal resolution of approximately 15 s and 200 m (e.g., Tridon et al., 2013; Giangrande et al., 2013). To align with the 5 min disdrometer measurements, an RWP profile from the midpoint of the 5 min window is selected. RWP measurements are typically stable with respect to $Z$ calibration offsets, with measurements aligned with those from the surface disdrometer (typically viable to within 2 dB). Echo-top height (ETH) from the RWP is defined as the altitude at which column $Z$ drops below 10 dBZ. Amazon RWP observations indicate this relative $Z$ altitude as the approximate height that mean convective cloud vertical velocity approaches $0\,\mathrm{m\,s^{-1}}$. Vertical air velocity retrievals and echo classifications follow techniques outlined by Giangrande et al. (2016b). For echo classifications, we identify convective and stratiform regions on the basis of column $Z$ signatures, velocity properties and/or so-called radar "bright band" (melting-level) designations for longer wavelengths (e.g., Fabry and Zawadzki, 1995; Williams et al., 1995; Geerts and Dawei, 2004). In contrast to scanning radar-based echo designations (e.g., those typically use near-surface $Z \simeq 40$–$45$ dBZ thresholds; e.g., Steiner et al., 1995), one RWP advantage is that columns exhibiting stronger vertical air velocity signatures help to differentiate transitional or elevated convective cells (e.g., instances of $|VV| > 2\,\mathrm{m\,s^{-1}}$).

### 2.2 ARM T3 aerosol observations and aerosol regime classification

Aerosol regime classifications are based on the combination of number concentration of particle CN measurements, measurements for the fraction of particles with diameters less than 70 nm, and carbon monoxide CO and oxides of nitrogen ($NO_y$) measurements at the T3 location using instrumentation as described in Thalman et al. (2017) and the Supplement. The philosophy for this aerosol classification is that each aerosol measurement builds on the previous when establishing a background condition ("clean"), with additional support for "polluted" conditions (e.g., urban, above this background condition) as well as "biomass burning" conditions attributed on top of "polluted" criteria. One advantage for using this classification is that this combination of measurements helps mitigate concerns that precipitation onset will mask ambient aerosol conditions (e.g., as in including an insoluble CO measurement). Because of the pronounced shift in aerosol properties seasonally, the methods subclassify background and polluted air mass types according to seasonal-specific windows. Classifications are available at 5 min intervals that align with the available precipitation observations.

As summarized by Thalman et al. (2017), clean conditions (typical background levels) exhibit values of $\mathrm{CN} < 500\,\mathrm{cm^{-3}}$, $\mathrm{CO} < 0.14$ ppm and $\mathrm{NO}_y < 1.5$ ppbv during the wet season. In contrast, background levels shift towards values of $\mathrm{CN} \simeq 1500\,\mathrm{cm^{-3}}$ (e.g., potentially a 3 or more factor of difference in CN) for similar CO and $\mathrm{NO}_y$ thresholds during the dry season (transitional months fall between wet and dry characteristics). In this regard, the dry season background conditions reflect regional biomass burning background levels that might otherwise be considered polluted conditions during typical wet season months. For this study, sampling limitations during the GoAmazon2014/5 dry season (lack of available collocated precipitation and aerosol measurements) requires our use of only wet season observations to provide a more detailed aerosol–cloud–precipitation

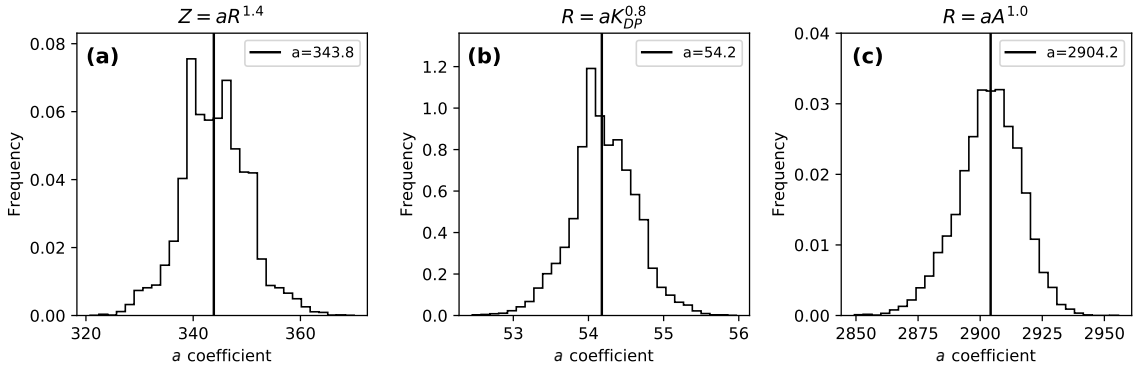


**Figure 1.** Histograms for $a$-coefficient values from single-parameter rainfall relationships **(a)** $R(Z)$, **(b)** $R(K_{DP})$ and **(c)** $R(A)$, calculated using the least-squares method under the assumption of a fixed $b$ coefficient from random sampling of half of the dataset (5000 times), for the S-band wavelength. The black vertical lines represent the $a$ coefficient calculated based on the whole dataset.

investigation. Under wet season conditions, polluted regimes are those having CN $> 500\,\mathrm{cm}^{-3}$. Biomass regimes are considered a more stringent polluted classification, classified as those polluted regimes that also have CO $> 0.14$ ppm.

### 2.3 PARSIVEL sampling and rainfall relationship interpretation

Later sections document relationships between estimated radar quantities and the measured rainfall rate $R$. These quantities carry instrument sampling considerations that include catchment uncertainties under convective conditions (e.g., Duchon and Essenberg, 2001), additional limitations when compared to collocated devices (e.g., Tokay et al., 2013; Park et al., 2017; Thurai et al., 2017) and/or processing assumptions when applying functional-form DSD parameter fits (e.g., Smith et al., 2009; Cao and Zhang, 2009). Radar quantities as estimated using the disdrometer are also influenced by raindrop shape and additional assumptions introducing variability established in previous studies (e.g., Thurai et al., 2007). Given our comparisons among rainfall accumulations with surface gauge measurements under typical storm intensities, as well as previous side-by-side performance testing of other PARSIVEL units, we do not anticipate radar quantity uncertainty falling outside the variability established by previous studies. For example, reasonable instrument offsets for radar quantities such as $Z$ may be on the order of 10–20 % or 1–2 dBZ.

An additional consideration when fitting rainfall relationships is the representativeness of this dataset, including challenges when attempting to establish the significance of functional fits. We establish coefficients for conventional $R(Z)$ relationships of the form $Z = aR^b$ using nonlinear least-squares methods matched over the entire dataset (or subsets) of $Z$–$R$ pairs. For lengthier datasets, it is informative to test variability in coefficients as related to modest samples drawn from the total population. Since consecutive DSD observations within precipitation events are nonindependent and correlated in processes (e.g., Lee et al., 2009), it may be important to consider this impact of proper spacing among samples when ensuring a reliable relationship.

As plotted in Fig. 1, we show histograms for $a$-coefficient values from various single parameter rainfall relationships (radar quantities estimated as in previous sections), assuming a fixed $b$ coefficient as determined from our complete Amazon dataset for the S-band wavelength. This example highlights the sensitivity in the $a$ coefficients as estimated from random half-dataset subsets to the complete dataset (vertical black line). Assuming a constant $b$ coefficient of $\simeq 1.4$ is typically a reasonable assumption to assist in microphysical interpretation from $R(Z)$ relationships for size-controlled conditions (e.g., Steiner et al., 2004). As the radar wavelength decreases, the sampling sensitivity depends on the radar quantity of interest. For example, the differences we observe for Amazon subsamples are typically to within 5 % of the mean dataset $a$-coefficient value with respect to $R(Z)$. Though not shown in Fig. 1, a deterioration in performance at shorter wavelengths is found for $R(Z)$ relationships owing to the importance of larger diameters to $Z$ estimates and increased non-Rayleigh scattering. In contrast, $a$ coefficients are found typically to within 2 % for $R(K_{DP})$ and $R(A)$ relations, with improved performance to shorter wavelengths (more immediate relationship between these quantities and rainfall rate). Such results help inform basic interpretations of the significant changes (larger than that expected from subsampling) in these radar relationship coefficients. The corresponding plots for C-band and X-band wavelengths are provided in the Supplement (Figs. S1 and S2).

## 3 Summary precipitation results and interpretation for retrieval methods

This section summarizes bulk precipitation properties, rainfall relationships and basic dual-polarization radar connections for the GoAmazon2014/5 dataset. A summary of DSD

**Table 1.** A summary of 5 min DSD parameter breakdowns for number of DSDs, rain rate $R$, median volume drop size $D_0$, normalized DSD intercept parameter $N_w$, reflectivity $Z$ at S-band wavelengths, and liquid water content (LWC), filtered according to rainfall rate intervals, for all, wet and dry seasons for the Amazon (MAO) and the Southern Great Plains (SGP) sites.

| $R$ (mm h$^{-1}$) | No. DSD | | $< R >$ (mm h$^{-1}$) | | $< D_0 >$ (mm) | | $< N_w >$ (m$^3$ mm$^{-1}$) | | <Z>(dBZ) | | $<$ LWC $>$ (g m$^{-3}$) | |
|---|---|---|---|---|---|---|---|---|---|---|---|---|
| All (total rainfall = 2597 mm for MAO dataset, 694 mm for SGP dataset) | | | | | | | | | | | | |
| | MAO | SGP | MAO | SGP | MAO | SGP | MAO | SGP | MAO | SGP | MAO | SGP |
| 0.5–2 | 1080 | 676 | 1.15 | 1.17 | 1.01 | 0.97 | 6580 | 8882 | 24.1 | 24.1 | 0.08 | 0.08 |
| 2–4 | 582 | 337 | 2.86 | 2.87 | 1.24 | 1.26 | 6525 | 4718 | 30.5 | 30.9 | 0.17 | 0.15 |
| 4–6 | 294 | 148 | 4.83 | 4.83 | 1.34 | 1.46 | 7621 | 4454 | 33.7 | 34.7 | 0.27 | 0.23 |
| 6–10 | 292 | 116 | 7.66 | 7.56 | 1.49 | 1.73 | 7445 | 3873 | 36.5 | 38.5 | 0.39 | 0.34 |
| 10–20 | 339 | 85 | 14.61 | 14.29 | 1.70 | 1.95 | 6913 | 4333 | 40.8 | 42.3 | 0.69 | 0.61 |
| 20–40 | 289 | 61 | 27.79 | 28.48 | 1.90 | 2.16 | 6948 | 4543 | 44.9 | 45.9 | 1.21 | 1.08 |
| 40–60 | 93 | 19 | 48.95 | 47.89 | 2.07 | 2.24 | 7699 | 5502 | 48.4 | 49.0 | 2.03 | 1.82 |
| Wet season (total rainfall = 1245 mm for MAO dataset) | | | | | | | | | | | | |
| 0.5–2 | 649 | | 1.14 | | 0.99 | | 6892 | | 23.7 | | 0.08 | |
| 2–4 | 301 | | 2.88 | | 1.19 | | 7851 | | 30.1 | | 0.17 | |
| 4–6 | 148 | | 4.80 | | 1.33 | | 8933 | | 33.5 | | 0.27 | |
| 6–10 | 147 | | 7.73 | | 1.49 | | 8295 | | 36.1 | | 0.39 | |
| 10–20 | 162 | | 14.78 | | 1.65 | | 8149 | | 40.4 | | 0.72 | |
| 20–40 | 147 | | 27.57 | | 1.86 | | 7666 | | 44.7 | | 1.23 | |
| 40–60 | 44 | | 49.02 | | 2.04 | | 8547 | | 48.1 | | 2.05 | |
| Dry season (total rainfall = 366 mm for MAO dataset) | | | | | | | | | | | | |
| 0.5–2 | 73 | | 1.19 | | 1.06 | | 4453 | | 24.9 | | 0.08 | |
| 2–4 | 33 | | 2.79 | | 1.32 | | 4694 | | 30.9 | | 0.15 | |
| 4–6 | 24 | | 4.76 | | 1.29 | | 7417 | | 33.1 | | 0.27 | |
| 6–10 | 31 | | 7.72 | | 1.53 | | 5045 | | 37.7 | | 0.38 | |
| 10–20 | 34 | | 14.92 | | 1.89 | | 4151 | | 42.5 | | 0.65 | |
| 20–40 | 30 | | 28.60 | | 2.13 | | 4275 | | 46.4 | | 1.16 | |
| 40–60 | 14 | | 49.35 | | 2.24 | | 5349 | | 49.3 | | 1.93 | |

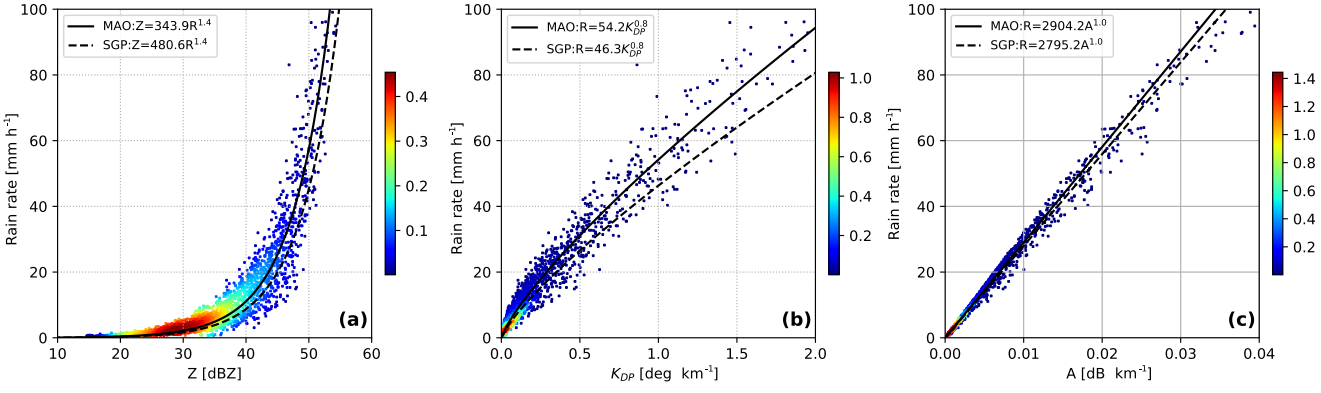


**Figure 2.** Scatter plots of **(a)** $Z$, **(b)** $K_{DP}$ and **(c)** $A$ versus rain rate and overlaid associated relationship fits using the least-squares method for the Amazon (MAO, solid lines) and SGP-Oklahoma (SGP, dashed lines) sites, for the S-band wavelength. Density is shown on the color scale.

parameter breakdowns for select quantities, filtered according to rainfall rate intervals, is located in Table 1. As one point of comparison to continental expectations, we include values obtained from a year-long ARM Southern Great Plains (SGP) PARSIVEL2 deployment (November 2016 through October 2017), processed similarly to the Amazon datasets. Within these narrowed rainfall rate intervals, the Amazon precipitation exhibits reduced median drop sizes

**Table 2.** Radar rainfall and self-consistency relations for the GoAmazon2014/5 dataset, for the cumulative dataset with all, wet and dry seasons, and convective and stratiform precipitation based on RWP classifications. Coefficients estimated at S-, C- and X-band radar wavelengths.

| Wavelength | | $R(Z)$ ($T = 20\,^{\circ}$C) | $R(K_{DP})$ ($T = 20\,^{\circ}$C) | $R(A)$ ($T = 20\,^{\circ}$C) | $R(A)$ ($T = 10\,^{\circ}$C) |
|---|---|---|---|---|---|
| S band | All | $Z = 343.9R^{1.4}$ | $R = 54.2K_{DP}^{0.8}$ | $R = 2904.2A^{1.0}$ | $R = 2227.6A^{1.0}$ |
| | Wet season | $Z = 329.5R^{1.4}$ | $R = 55.2K_{DP}^{0.8}$ | $R = 2949.6A^{1.0}$ | $R = 2265.1A^{1.0}$ |
| | Dry season | $Z = 388.3R^{1.4}$ | $R = 51.5K_{DP}^{0.8}$ | $R = 2732.3A^{1.0}$ | $R = 2090.5A^{1.0}$ |
| | Convective | $Z = 339.9R^{1.4}$ | $R = 54.6K_{DP}^{0.8}$ | $R = 2895.0A^{1.0}$ | $R = 2219.6A^{1.0}$ |
| | Stratiform | $Z = 385.8R^{1.4}$ | $R = 51.1K_{DP}^{0.8}$ | $R = 2867.1A^{1.0}$ | $R = 2202.0A^{1.0}$ |
| C band | All | $Z = 289.0R^{1.4}$ | $R = 30.6K_{DP}^{0.8}$ | $R = 287.8A^{0.9}$ | $R = 239.4A^{0.9}$ |
| | Wet season | $Z = 280.6R^{1.4}$ | $R = 31.3K_{DP}^{0.8}$ | $R = 314.4A^{0.9}$ | $R = 258.3A^{0.9}$ |
| | Dry season | $Z = 314.8R^{1.4}$ | $R = 28.5K_{DP}^{0.8}$ | $R = 242.1A^{0.9}$ | $R = 203.4A^{0.9}$ |
| | Convective | $Z = 281.6R^{1.4}$ | $R = 30.7K_{DP}^{0.8}$ | $R = 278.4A^{0.9}$ | $R = 232.3A^{0.9}$ |
| | Stratiform | $Z = 339.8R^{1.4}$ | $R = 29.5K_{DP}^{0.8}$ | $R = 290.6A^{0.9}$ | $R = 239.7A^{0.9}$ |
| X band | All | $Z = 261.4R^{1.6}$ | $R = 21.5K_{DP}^{0.8}$ | $R = 41.4A^{0.8}$ | $R = 43.0A^{0.8}$ |
| | Wet season | $Z = 239.1R^{1.6}$ | $R = 21.6K_{DP}^{0.8}$ | $R = 42.7A^{0.8}$ | $R = 43.9A^{0.8}$ |
| | Dry season | $Z = 303.2R^{1.6}$ | $R = 21.1K_{DP}^{0.8}$ | $R = 38.2A^{0.8}$ | $R = 40.0A^{0.8}$ |
| | Convective | $Z = 250.2R^{1.6}$ | $R = 21.6K_{DP}^{0.8}$ | $R = 41.0A^{0.8}$ | $R = 43.0A^{0.8}$ |
| | Stratiform | $Z = 318.5R^{1.6}$ | $R = 19.6K_{DP}^{0.8}$ | $R = 40.8A^{0.8}$ | $R = 41.3A^{0.8}$ |
| Self-consistency ($T = 20\,^{\circ}$C) | | | | | |
| S band | All | $Z = 45.6 + 10.04\log(K_{DP}) + 3.20Z_{DR}$ | | | |
| | Wet season | $Z = 45.7 + 10.10\log(K_{DP}) + 3.17Z_{DR}$ | | | |
| | Dry season | $Z = 45.6 + 10.05\log(k_{DP}) + 3.16Z_{DR}$ | | | |
| C band | All | $Z = 43.3 + 10.12\log(K_{DP}) + 1.96Z_{DR}$ | | | |
| | Wet season | $Z = 43.3 + 10.18\log(K_{DP}) + 1.94Z_{DR}$ | | | |
| | Dry season | $Z = 43.4 + 10.12\log(K_{DP}) + 1.82Z_{DR}$ | | | |
| X band | All | $Z = 38.6 + 9.54\log(K_{DP}) + 4.62Z_{DR}$ | | | |
| | Wet season | $Z = 38.7 + 9.54\log(K_{DP}) + 4.52Z_{DR}$ | | | |
| | Dry season | $Z = 38.7 + 9.80\log(K_{DP}) + 4.89Z_{DR}$ | | | |

and higher drop concentrations. This change is also reflected in lower $Z$ values and higher LWC for a similar $R$ compared to SGP observations. Although the 5 min dry season samples are limited, rainfall rate breakdowns demonstrate the dry season exhibits higher relative $Z$ and median drop sizes (lower $N_w$ and LWC) compared to wet season observations. Discrepancies between SGP and the Amazon, as well as wet–dry separations, are most pronounced at the higher $R$ consistent with convective cores. This is likely based on the propensity for observing melting hail in deeper SGP convection and/or observed larger melting aggregates in stratiform regions trailing convective lines. Both SGP situations would favor sampling larger drop sizes at the surface.

### 3.1 Single-parameter dual-polarization rainfall relationships at S-, C- and X-band wavelengths

In Fig. 2, we plot summary dataset scatter plots overlaid with dual-polarization relationship fits for the S-band wavelength. The corresponding plots for the C- and X-band wavelengths are provided in the Supplement (Figs. S3 and S4). A summary of matched rainfall coefficients is provided in Table 2. For these tables, $b$ coefficients were fixed at a characteristic dataset value to facilitate comparison across regime breakdowns. In Fig. 2, we overlay the associated fitting (dashed lines) from SGP-Oklahoma to provide a continental reference. As a function of radar wavelength, the $a$-coefficient values decrease as wavelength decreases (e.g., quantities more closely related to the rainfall rate). SGP dual-polarization relationships are consistent with previous studies (e.g., Giangrande et al., 2014b), providing confidence in the appropriateness of disdrometer processing. Note that minor discrepancies in SGP $R(Z)$ relations may be related to our filtering of large drops > 5 mm that disproportionately influence $Z$ measurements at sites including SGP wherein melting hail is more regularly observable. Moreover, SGP relations may carry higher $a$ coefficients (thus, larger discrepancies with the Amazon relationships) than reported in our Table 2.

Summarized Amazon relationships follow a tropical expectation (more significant role for warm-rain processes,

e.g., droplet growth via collision–coalescence), indicating higher concentrations of smaller drops. This is observed with a smaller $a$ coefficient than found for SGP $R(Z)$ relations and larger $a$ coefficients than found for SGP $R(K_{DP})$ and $R(A)$ relations (as in Fig. 2). These changes reflect a significant change when viewed compared to Amazon dataset sampling arguments found in Sect. 2. For Table 2, $R(A)$ relationships are also listed for multiple temperature assumptions, highlighting one explanation for modest variability when attempting to promote these relations for practical rainfall retrievals (e.g., Ryzhkov et al., 2014; Giangrande et al., 2014b). As additional reference for dual-polarization radar processing and natural calibration concepts, self-consistency relationships among radar quantities $K_{DP}$, $Z$ and $Z_{DR}$ for the various wavelengths have been provided in Table 2. In comparison to continental SGP references for statistical DSD relationships (e.g., Ryzhkov et al., 2005), self-consistency coefficients in Table 2 reinforce the tropical character of the Amazon precipitation, again consistent with smaller median drop sizing (e.g., reductions in $Z_{DR}$ or $K_{DP}$) to achieve similar estimates of $Z$.

Rainfall relationships stratified according to wet and dry season conditions are also found in Table 2. The wet season indicates lower $a$ coefficients for $R(Z)$ and higher relative coefficients for $R(K_{DP})$ and $R(A)$ relations. One interpretation is that for similar $R$ values, the wet season DSDs carry more pronounced tropical precipitation characteristics. A similar trend is found with seasonal self-consistency relationship breakdowns. As before, most seasonal breakdowns are reflected as significant changes in relationship coefficients when compared with the sampling arguments in Sect. 2. An exception to this are $K_{DP}$-based rainfall relationships that appear least sensitive to this seasonal DSD variability at X-band wavelengths (the shortest wavelength tested), possibly a reflection of non-Rayleigh influences on $K_{DP}$ (i.e., the presence/absence of larger drops) is less important.

Finally, interpreting seasonal differences can be challenging without mentioning factors including storm intensity changes related to the larger-scale thermodynamic shifts that alter convective and congestus frequency, or mid-level moisture (e.g., during GoAmazon2014/5 as in Giangrande et al. (2017), cf. Fig. 2). The dry season promotes events that achieve a higher rainfall rate $R$, but under convective environments that favor enhanced evaporation, cooling and subsidence, which are less capable of sustaining expansive stratiform processes. Wet and transitional month stratiform precipitation linked to aggregation and associated DSD evolution processes beneath the melting layer favors lower $N_w$, higher $D_0$ values for similar $Z$ values (e.g., Giangrande et al., 2016a). The fraction of stratiform DSDs (count) of the total DSD observations in this dataset for the wet season is 50.5 %. This fraction decreases to approximately 30.1 % for the dry season. Nevertheless, summary rainfall properties skew heavily towards convective designations for all seasons, as reported in Table S1. Seasonal changes will be discussed further in Sect. 4 in the context of multiparameter DSD breakdowns.

### 3.2 Convective–stratiform regimes for rainfall relationships and DSD properties

Isolating contributions from convective and stratiform DSDs is an initial step for improved rainfall estimates or possible model evaluation (e.g., Tokay and Short, 1996). Table 2 is segregated according to RWP-based convective–stratiform echo classifications. These RWP-based segregations will be further decomposed in Sect. 4 but for demonstration purposes are considered a reasonable benchmark when isolating bulk regime contributions. Cumulative contoured frequency altitude display histograms (e.g., Yuter and Houze, 1995, CFADs) with quantile values (median and 90th and 95th percentiles) for RWP $Z$ and vertical velocity retrieval profiles are plotted in Fig. 3. These histograms help establish these RWP classifications as reasonable; for example, convective columns (Fig. 3a, c) have monotonically decreasing profiles and stronger vertical motions, whereas stratiform (Fig. 3b, d) columns emphasize pronounced radar bright band – or, aggregation process signatures and weaker composite upwards vertical air velocity signatures (e.g., Fabry and Zawadzki, 1995). Given that checks for pronounced bright band signatures are part of the echo classification, that these signatures are observed is not surprising. Inflation of mid-level downwards motions in stratiform regions is observed near the freezing level, originating from contamination within the melting layer on fall speed corrections (e.g., enhanced $Z$ from aggregation resulting in overestimates for ice fall speeds).

In terms of rainfall relationships in Table 2, convective relationships demonstrate higher coefficient values for $R(K_{DP})$ relations and smaller coefficients for $R(Z)$ relations. This shift is consistent with convection favoring high $N_w$ and low $D_0$ for a similar $Z$ or $K_{DP}$. $R(A)$ relationships register as those least influenced by these separations (smallest coefficient shifts), followed by $K_{DP}$ relationships at the shorter wavelengths. This reduced coefficient variability reflects on the closer relationship between $A$ and $K_{DP}$ with rainfall rate, less influenced by the presence/absence of select larger drop sizes. As complementary examples for the Amazon datasets, in Fig. 4 we show the corresponding histograms for Amazon convective and stratiform DSDs in terms of $N_w$ (Fig. 4a), LWC versus $R$ relationships (Fig. 4b) and $D_0$ variations with $Z$ (Fig. 4c). For these plots, convection is noted by red shadings and stratiform is plotted in blue contours. Convection demonstrates a broader distribution of $N_w$, LWC and other quantities of interest. Although there is substantial overlap with stratiform DSDs, convective DSDs exclusively cover higher extreme parameter spaces.

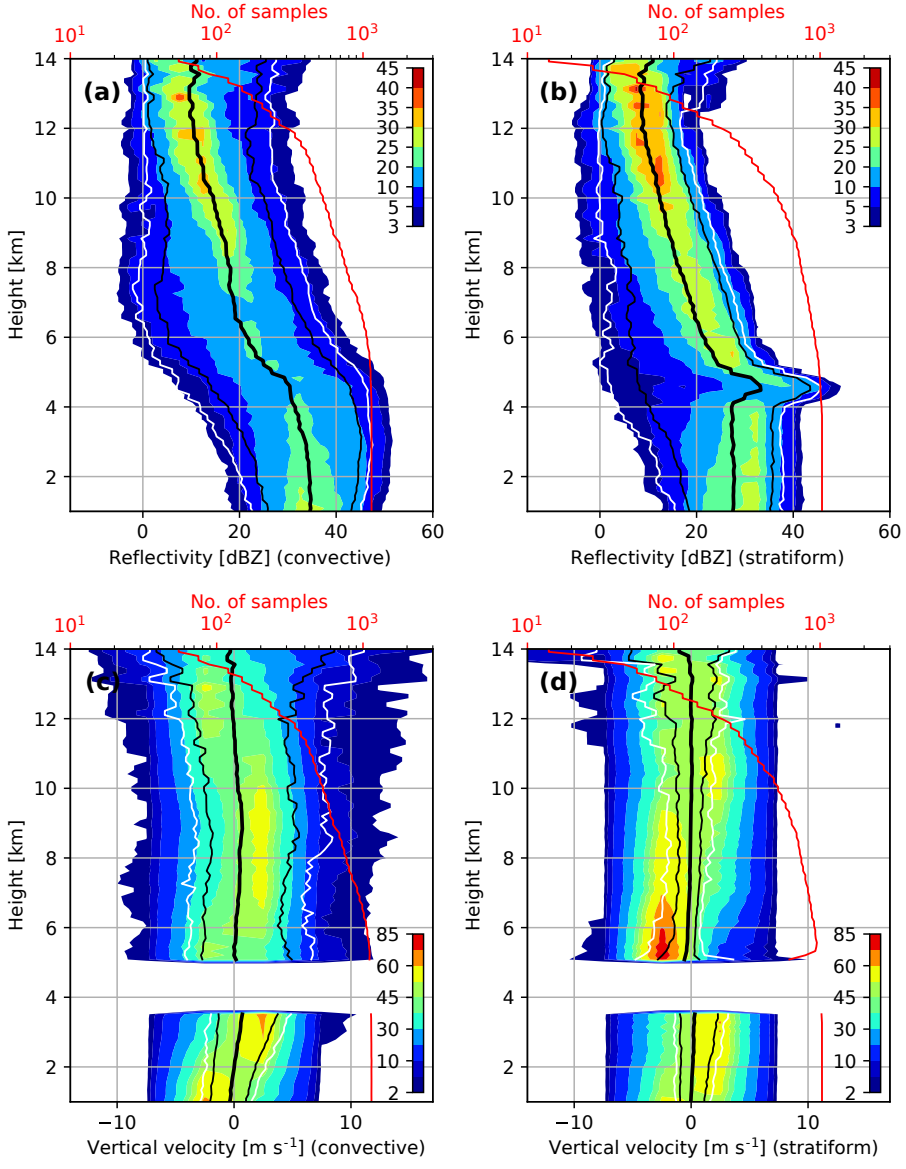


**Figure 3.** Contoured frequency altitude display (CFAD) histograms for the entire Amazon dataset with confidence intervals, the median (thick black lines) and 90th (thin black lines) and 95th percentiles (white lines) for RWP convective and stratiform reflectivity profiles **(a, b)** and vertical velocity retrievals **(c, d)**. The number of profiles of each situation is shown as a red line.

## 4 Amazon precipitation properties: cumulative dataset characteristics

Convection-permitting models struggle to simultaneously capture convective and stratiform cloud processes; therefore model–observational comparisons often emphasize bulk cloud regime segregations and contingent performances to diagnose issues with cloud model treatments (e.g., Lang et al., 2003). Although there is no clear line separating convective and stratiform processes (e.g., for identifying deficiencies in modeled precipitation, vertical air motions or heating profiles), bulk regime separations introduced for Sect. 3 are of practical use. Here, we assess how precipitation depictions from previous campaigns might be useful to constrain Amazon observations and the sensitivity of radar quantities to those changes.

Precipitating clouds identified by the RWP demonstrate a clear bimodal ETH distribution (Fig. 5), and one that varies according to Amazon seasons (Fig. 5a). The behaviors are consistent with freezing level (typically around 5 km above surface) and tropopause-level cloud-top expectations for tropical convection (Fig. 5b, e.g., Johnson et al., 1999; Jensen and Del Genio, 2006). Note also that the RWP is not sensitive to cloud-sized particles; thus actual cloud-top

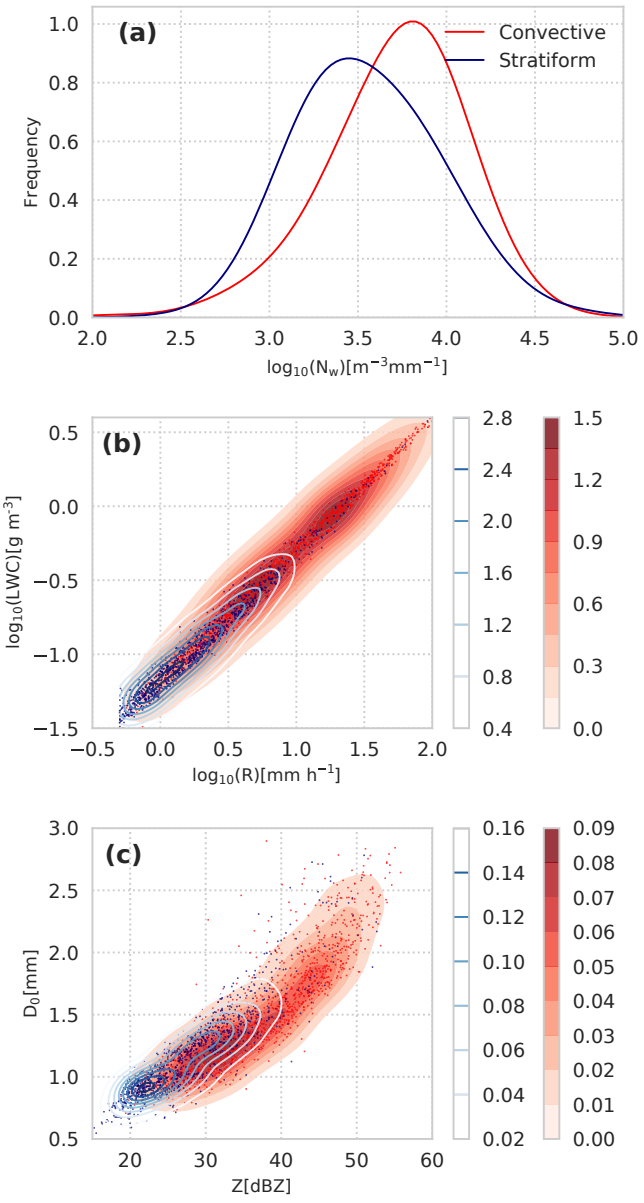


**Figure 4.** Histograms associated with RWP classification-based convective (red) and stratiform (blue) DSDs in terms of $N_w$ **(a)**, LWC versus $R$ behaviors **(b)** and $D_0$ scaling according to $Z$ **(c)**. Density is shown on the color scale.

heights (as from collocated cloud radar references) may extend 2 km or more above these heights. Sounding-based winds over the T3 site are predominantly easterly (mostly observed during the dry season) to northeasterly (mostly wet season) (Fig. 5c). Low-level $Z$ observations (Fig. 5d) illustrate that Amazon cumuli are often linked to relatively modest values of $Z \simeq 35$ dBZ. From a practical radar-based classification perspective that typically utilizes higher $Z \simeq 40$–45 dBZ thresholds, it follows that standard methods may necessitate additional texture, peakedness or similar ideas to properly identify Amazon convection (e.g., Steiner et al., 1995).

As documented by Giangrande et al. (2017) (Figs. 6 and 8), convection passing over T3 follows a diurnal cycle with peak cloud frequency around local 13:00–14:00 LT. A shift in peak frequency to later afternoon is found within the dry season, whereas wet season deeper convection exhibits a secondary peak in cloud frequency (related to mesoscale convective systems) during the overnight hours. Congestus clouds (loosely precipitating clouds having ETHs between 4.5 and 9 km) demonstrate a similar diurnal pattern across all Amazon seasons. The frequency of all precipitating clouds (congestus and deeper) increases substantially for the Amazon wet season. Of additional note, the precipitation originating from congestus or possible shallower forms of tropical organized cloud systems (as defined solely on an RWP-based ETH < 9 km in Chen and Liu, 2015) is nontrivial for this Amazon dataset (accumulations as reported in Table S1 in the Supplement).

As plotted in Fig. 6, we show the frequency for observing various levels of vertical air motions within an RWP column as additional reference to the convective character of these clouds. Displays present these frequencies as a function of a lower-level RWP $Z$ ($\simeq 2$ km). To lower ranges of $Z$ ($< 35$ dBZ), we observe a stable percentage of columns having vertical air motions around 1 ms$^{-1}$. This may also be viewable as the baseline uncertainty regarding RWP-based vertical velocity retrievals. As $Z$ increases above 35 dBZ, we observe a rapid increase in the frequency of stronger updrafts and downdrafts, indicative of the increasing contributions from convective clouds sharing these relative $Z$ levels. As $Z$ is stronger, the likelihood of sampling deeper clouds (and therefore the additional chance to observe a stronger velocity in those columns) will also increase as a function of $Z$. The results in Fig. 6 also provide some guidance in convective–stratiform classification methods for scanning radars that use low-level Z thresholds (e.g., Steiner et al., 1995). Specifically, low-level $Z$ exceeding a 40 dBZ value (or higher) is a reasonable designation of convection in the absence of vertical velocity measurements.

### 4.1 Disdrometer convective–stratiform segregation: alignment with RWP signatures

In Fig. 7, a convective–stratiform regime segregation concept is shown, with the solid line as reference to a DSD-based classification following Bringi et al. (2003) (herein BR). In this $N_w$ versus $D_0$ space, BR proposed that tropical maritime convective precipitation observed at Darwin, Australia, falls to the right of the solid black line in Fig. 7. In terms of thresholds, for this dataset the DSDs best aligned with falling on either side of the BR line correspond to those having a rainfall rate threshold of 13 mm h$^{-1}$, or a $Z$ value of 40 dBZ. In Fig. 7, we also overlay the contours of the RWP-based classifications for convective (red colors) and stratiform (blue

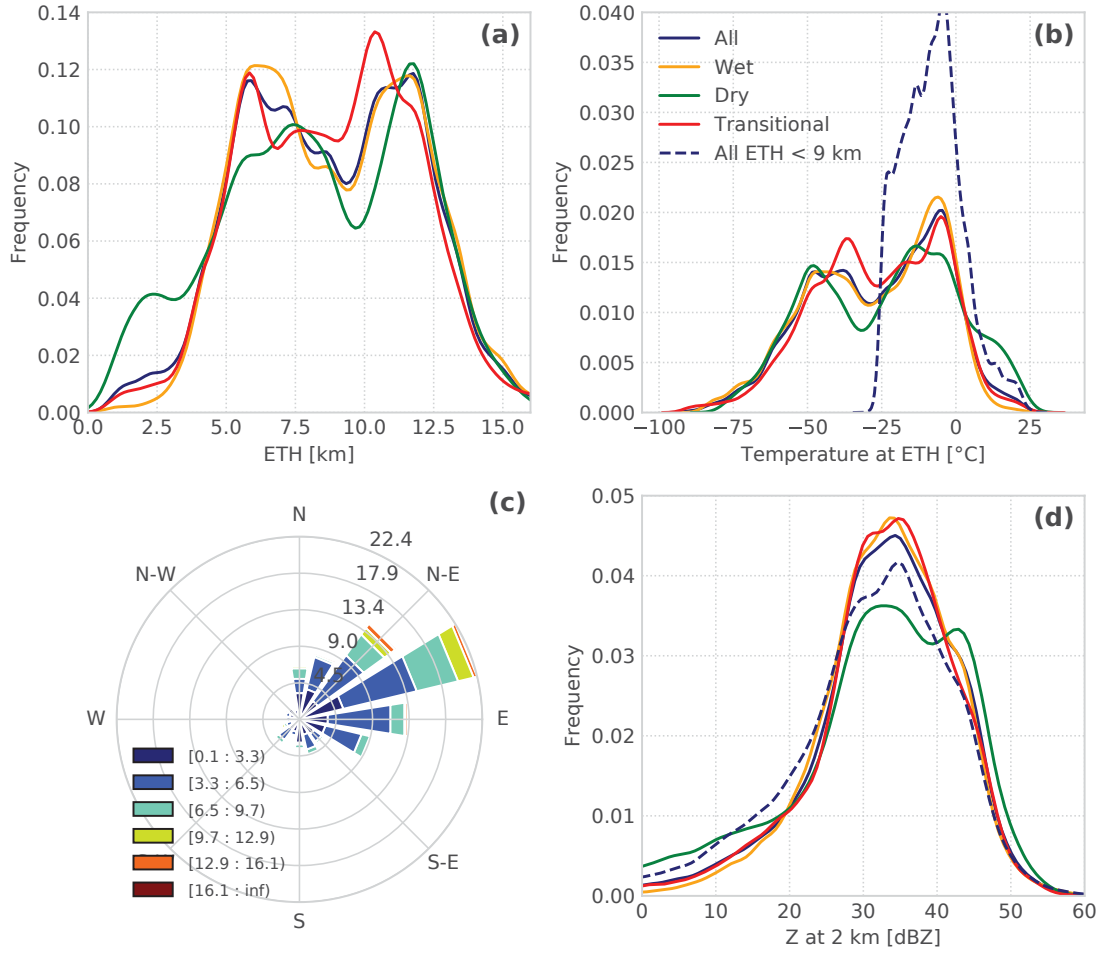


**Figure 5.** Histograms associated with RWP classification-based convective DSDs in terms of ETH **(a)**, temperature at ETH **(b)** and $Z$ at 2 km **(d)** for all, dry, wet and transitional seasons, as well as the congestus for all the seasons. The wind rose **(c)** is also shown for all the seasons.

lines) precipitating columns. The ellipse in Fig. 7 indicates the two-sigma confidence interval for those regions containing stratiform DSDs based on the RWP classification.

RWP-based classifications indicate that substantial DSDs may be attributed to convective classifications left of this BR line. These are associated with the RWP identifying congestus or shallower convective cloud columns, as based on velocity signatures. However, the Amazon dataset supports bulk BR findings for deeper tropical convection in that precipitation to the right of the BR line is exclusive to convective designations. Since BR was developed using a Darwin monsoonal dataset, we anticipate that the study included modest convective diversity, including congestus clouds, and clouds with maritime, continental and deeper convective properties (those supporting additional graupel growth). Darwin may exhibit even more intense "Break" (e.g., more continental characteristics) convective cell periods and associated DSD changes interspersed with maritime tropical "Active" monsoonal conditions than what is observed over the Amazon (e.g., May and Ballinger, 2007; Dolan et al., 2013; Schumacher et al., 2015; Giangrande et al., 2014a, 2016b). However, it appears the use of BR would minimize the contributions from congestus or shallower organized convective precipitation found under Amazon conditions.

More recently, Thompson et al. (2015) highlighted limitations for imposing BR concepts when characterizing oceanic precipitation observed over ARM TWP ground disdrometers at Manus Island (Papua New Guinea) and equatorial Indian Ocean Gan (Addu Atoll, Maldives). Thompson et al. (2015) (herein TM) proposed a unique oceanic convective–stratiform segregation having origins in LWC and $D_0$ space. One justification for this change was to isolate DSD clusters exhibiting the higher concentrations of smaller drops consistent with oceanic convective clouds favoring warm-rain processes/collision–coalescence over mixed-phase and/or stratiform particle growth. The TM classification is simple to implement since it overlaps within the BR space as a line of constant $\log10(N_w) \simeq 3.85\,\mathrm{m}^{-3}\,\mathrm{mm}^{-1}$. As plotted in Fig. 8,

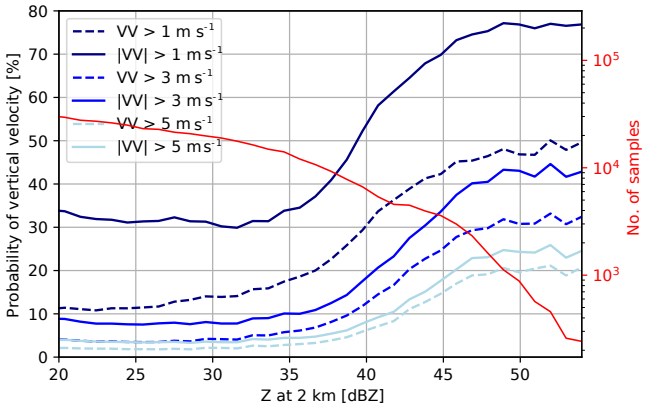


**Figure 6.** The frequency for observing a given vertical velocity (across all levels, $> 1\,\mathrm{ms}^{-1}$ in navy, $> 3\,\mathrm{ms}^{-1}$ in dark green, $> 5\,\mathrm{ms}^{-1}$ in light green) as a function of a 2 km RWP reflectivity. The number of samples (for $|VV| > 1\,\mathrm{ms}^{-1}$) is displayed as a red line.

we consider only the DSDs that would fall to the left of the BR separation line (e.g., those that follow a traditional BR stratiform designation). For this figure, the DSDs identified as belonging to convective or stratiform (based on the RWP definitions) are then subset according to the left and right panels, respectively. When populations from the Amazon DSDs exhibit more oceanic qualities (residing above the dashed TM line), contributions to the histograms (Fig. 8a, c) are typically associated with RWP convection signatures. Similarly, DSDs identified as stratiform by the RWP (Fig. 8b, d) follow those residing below the TM criteria for oceanic-like stratiform precipitation. Overall, bulk Amazon precipitation carries several hybrid characteristics as found from previous ARM tropical DSD studies.

### 4.2 Cumulative precipitation properties according to cloud regime and season

Extending the previous analysis into cloud regimes, in Fig. 9 we separate Amazon precipitation according to ETH values above and below 9 km. This choice follows the discussion from Fig. 5 and is assumed to be a reasonable proxy to also help separate statistical congestus from deeper convective events. These plots include combined convective precipitation (e.g., stronger updraft–downdraft regions) as well as associated trailing stratiform DSDs and/or decaying convection.

As shown in Fig. 9, deeper cumulus clouds are associated with an additional maritime continental DSD properties as is similar to Darwin studies, with fewer observations residing above TM recommendations for possible oceanic characteristics. Deeper convective and stratiform DSDs as designated by the RWP exhibit more frequent DSD examples having larger median drop sizes. In contrast, DSDs associated with ETH < 9 km carry DSD properties most similar to TM oceanic characteristics, having corresponding stratiform DSDs that favor smaller median drop sizing than deeper column counterparts. While tempting to attribute these oceanic ETH < 9 km DSD characteristics solely to weak, isolated congestus clouds, inspection of the events reveals oceanic DSDs are often associated with widespread convective lines and/or widespread convective cells (to be further discussed).

In Fig. 10, we show this cloud segregation according to dry, wet and transitional months (here, "transitional" implies May, October and November properties that share qualities of both wet and dry seasons). The dry season conditions (Fig. 10a, d) skew towards bulk precipitation properties associated with the deeper convective clouds from above. These properties follow an isolated, stronger convective cell expectation for dry season precipitation that also includes an absence of DSDs associated with detrained stratiform precipitation processes (e.g., low $N_w$, larger $D_0$) as discussed in the following section. In contrast, wet season DSD characteristics (Fig. 10b, e) follow previous tropical and oceanic expectations, with additional excursions into DSD contributions associated with the convective core modes (right of BR).

### 4.3 Stratiform precipitation properties associated with Amazon convective events

Stratiform precipitation within the Amazon is commonly observed during the wet season and transitional months, associated with the detrained regions from deeper convective cells or cell dissipation. Increased stratiform precipitation frequency during the wet season is attributed to factors including the seasonal change in midlevel moisture and reductions in wet season convective inhibition more supportive of convective initiation and prevalence. Recalling Fig. 8b and d, stratiform DSDs as identified by the RWP are often the same as combining thoughts from BR/TM recommendations. This statement is further confirmed consulting cumulative and fractional convective precipitation as in Table S1 in the Supplement. In Fig. 11, we present the composite DSD properties as reported in Fig. 9, exclusive to RWP-indicated stratiform properties. Contours overlaid in Fig. 11 indicate those DSD regions designated as having a bright band signature in the column. As for the left panels in Fig. 11 (ETH > 9 km), locations with profiles exhibiting clear bright band signatures correspond well with BR expectations for stratiform precipitation; for example, these would often represent the DSDs within more developed precipitation trailing deeper convective cells and mesoscale convective systems (e.g., Houze, 1997).

Lower echo-top stratiform characteristics (ETH < 9 km) indicate two unique clusters. The first cluster represents observations associated with aggregation processes that produce stronger melting layer signals, similar to examples with an ETH > 9 km. These observations are found under wet season conditions (50 % of the available DSDs), and are less common under dry season conditions (30 % of the available

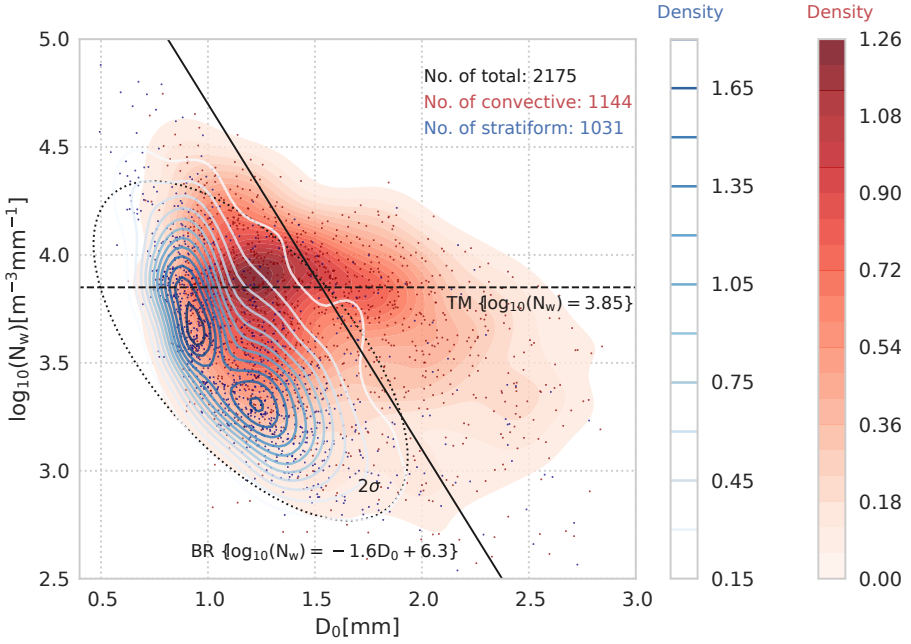


**Figure 7.** Scatter plot of $\log_{10}(N_w)$ versus $D_0$ from PARSIVEL disdrometer, overlaid by the contours representing the RWP-based classifications for convective (red colors) and stratiform (blue lines) precipitating columns. The ellipse conveys the two-sigma confidence interval (dotted line) for those regions containing RWP-based stratiform DSDs. The convective–stratiform regime segregation concepts in Bringi et al. (2003, BR) and in Thompson et al. (2015, TM) are presented as a solid black line and dashed black line, respectively.

DSDs). Initially, this supports an argument that enhanced wet season moisture influences sustained stratiform development, ice growth (deposition) and eventual aggregation processes. The second cluster is associated with smaller median drop sizes and higher relative number concentrations. This represents the more prevalent stratiform mode for lower-top dry season observations, and is equally frequent for wet season observations. This cluster argues for less developed stratiform processes, either owing to the lack of mid-level moisture in dry season profiles, or consistent with widespread, weaker wet season congestus (e.g., reduced inhibition resulting in larger areas having weaker updraft intensity).

### 4.4 Implications of convective–stratiform partitioning

Previous sections indicate that RWP and hybrid BR–TM classifications faithfully differentiate congestus and deeper convective DSDs from stratiform DSDs. Table S1 in the Supplement reports the total convective precipitation and fractional convective precipitation for this GoAmazon2014/5 dataset. These values are estimated according to segregations from BR methods, a hybrid BR–TM combination, the RWP classification, and a simple rainfall rate $R > 10\,\mathrm{mm\,h^{-1}}$ threshold. Table S1 in the Supplement has also been segregated according to wet/dry and transitional season component behaviors.

For the Amazon dataset, both TM–BR and RWP methods attribute approximately half of the total precipitation (convective plus stratiform) to possible congestus or shallower cloud regimes, as defined by our definitions with an ETH $< 9$ km. Moreover, we observe that the fractional convective precipitation is higher for those methods adding additional complexity to the classification. Convective fractions suggest differences to within $\simeq 10\,\%$. Seasonal breakdowns confirm that the wet season and transitional months are more dominated by stratiform rainfall, with transitional months suggesting the largest share of stratiform precipitation. Overall, fractional convective contributions are high (exceeding 80 %), but the strong agreement between RWP and BR–TM gives confidence that traditional radar segregations would report lower convective fractions owing to incorrect attribution of congestus or shallower-topped precipitation systems.

It is possible to check whether dual-polarization radar quantities are sensitive to apparent variations among congestus, deeper convection and associated stratiform precipitation properties. In Fig. 12, we show the ($Z$, $Z_{DR}$) scatter plot as well as ($K_{DP} - Z - Z_{DR}$) self-consistency curve behaviors for various regimes identified by the RWP; the lower panels in Fig. 12 illustrate the wet and dry season segregations. For all panels in Fig. 12, we present X-band dual-polarization estimates calculated from T-matrix scattering, as radar quantities at these shorter wavelengths should be more sensitive to lower rainfall rate conditions. The radar quantities are presented in terms of their associated two-sigma confidence regions (ellipses). Since radars routinely perform separate ETH and/or bright band designation checks, the

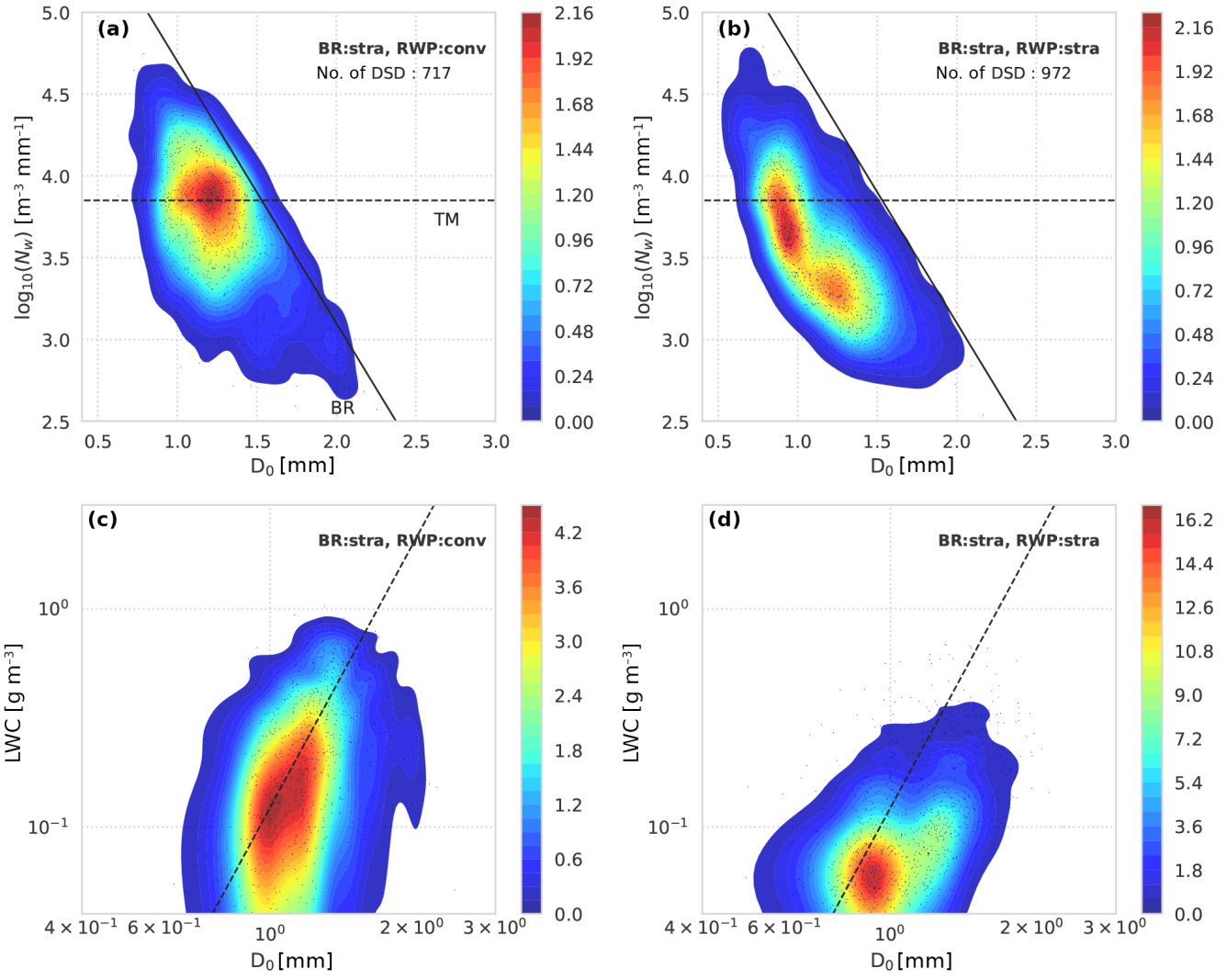


**Figure 8.** Scatter plots of $\log_{10}(N_w)$ versus $D_0$ and LWC versus $D_0$ for BR-based stratiform DSDs (density in colors). DSDs identified as convective and stratiform by the RWP are shown in **(a, c)** and **(b, d)**.

demonstrations in Fig. 12 are not a true reference for what is possible from a robust radar echo classification methodology. However, Fig. 12 suggests substantial overlap between these cloud precipitation regimes when placed in this dual-polarization context. This would suggest X-band or longer-wavelength radars would not be sufficient constraints for regime classifications without additional information. The most pronounced contrasts are those observed between wet and dry seasons, wherein the dry season favors the larger extremes for all dual-polarization radar quantities, associated with the contributions of larger drops.

## 5 Amazon precipitation properties: the Green Ocean characteristics

The Amazon wet season has been highlighted for its copious precipitation owing to factors including enhanced moisture and reduced convective inhibition (CIN). One additional consideration is that these conditions, possibly when coupled with cleaner atmospheric aerosol profiles, may promote the so-called Green Ocean or oceanic cloud and precipitation characteristics. In contrast, dry season convective conditions migrate towards enhanced convective available potential energy (CAPE) and stronger CIN that may promote stronger convective events, initiating within more polluted atmospheric states closer to continental regimes. Other recent Amazon studies indicate that the convection that initiates during the Amazon dry season exhibits more intense

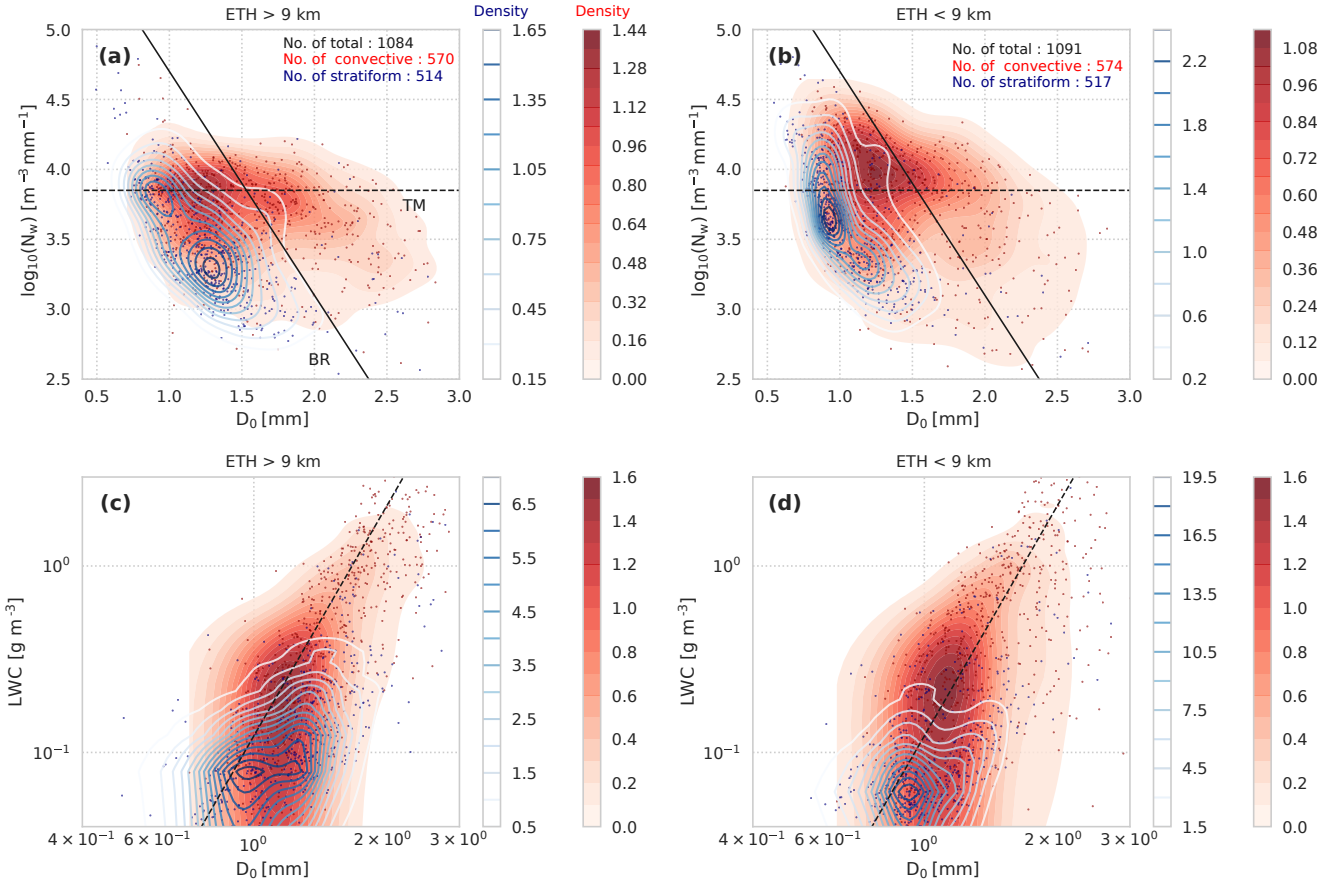


**Figure 9.** Scatter plots of $\log_{10}(N_w)$ versus $D_0$ and LWC versus $D_0$, overlaid by the contours representing the RWP-based classifications for convective (red colors) and stratiform (blue lines) precipitating columns and for ETH > 9 km **(a, c)** and ETH < 9 km **(b, d)** situations.

vertical air motions and precipitation properties (e.g., Giangrande et al., 2016b; Schiro, 2017).

### 5.1 The Amazon Green Ocean: when do we observe oceanic behaviors?

As shown in Fig. 13, we extend the previous analysis found in Fig. 10 to a seasonal comparison between deeper clouds (ETH > 9 km, reds) and congestus or shallower convection (ETH < 9 km, blues). To simplify, stratiform DSD components (as identified by the RWP) have been removed from this figure. Although all DSDs are assumed to be convective, it is instructive to focus on DSDs in Fig. 13 located to the right of the BR separation line, as those DSDs correspond to the most confident convective conditions having a typical rainfall rate $R > 13\,\mathrm{mm\,h^{-1}}$. As also in Table 1, convective dry season DSDs carry fewer drops, but larger median drop sizes. Physically, this corresponds well with expectations that stronger updrafts in the dry season should promote larger droplet sizes as a consequence of mixed-phase growth. Wet season characteristics are noticeably shifted towards higher number concentrations, with lower-relative LWC. This is consistent with the anticipated changes towards more oceanic and/or tropical warm-rain processes and cleaner and/or weaker updraft events. For dual-polarization radar studies, these characteristics are consistent with dry season convection exhibiting larger values in $Z_{DR}$ or $K_{DP}$ for a similar value of $Z$, noting surface conditions may also be modified slightly from the conditions sampled aloft from radar.

We show, in Fig. 14, congestus and deep convective full DSD averages for convective conditions as in Fig. 13. Average DSDs are also provided for those observations found to the right of the BR separation line, as well as those DSDs having $Z > 35$ dBZ. Overall, composite behaviors emphasize that dry season convective precipitation (and into convective core regions) is skewed towards an increased presence of larger drops, and toward parameter spaces favoring higher LWC for a similar $D_0$. In contrast to wet season properties, Amazon dry season precipitation conditions are not consistent with TM oceanic findings (shift towards DSDs having increased larger drops), though they do support that the updrafts in the dry season are stronger.

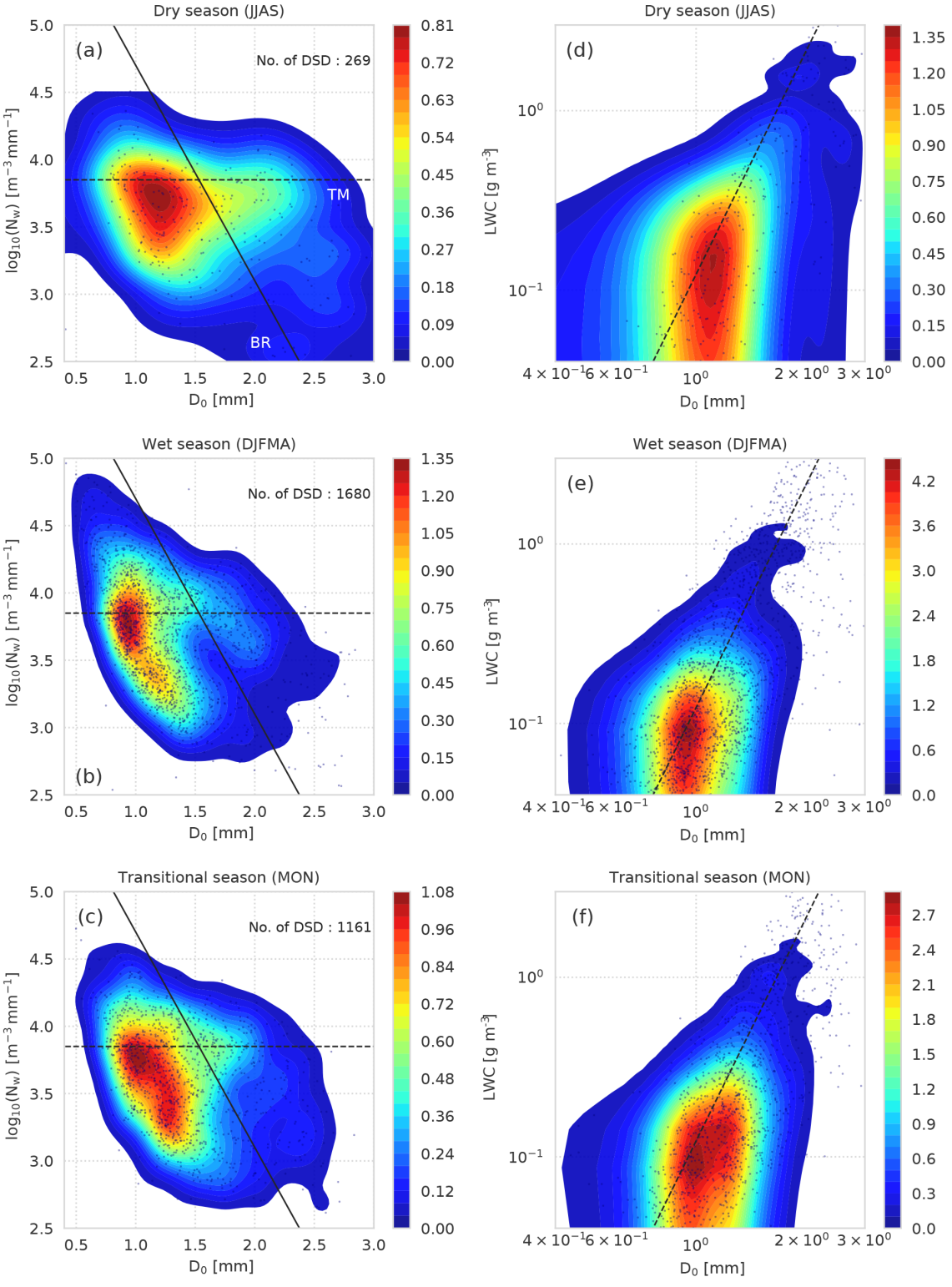


**Figure 10.** Scatter plots of $\log_{10}(N_w)$ versus $D_0$ and LWC versus $D_0$ for dry **(a, d)**, wet **(b, e)** and transitional **(c, f)** seasons (density in colors).

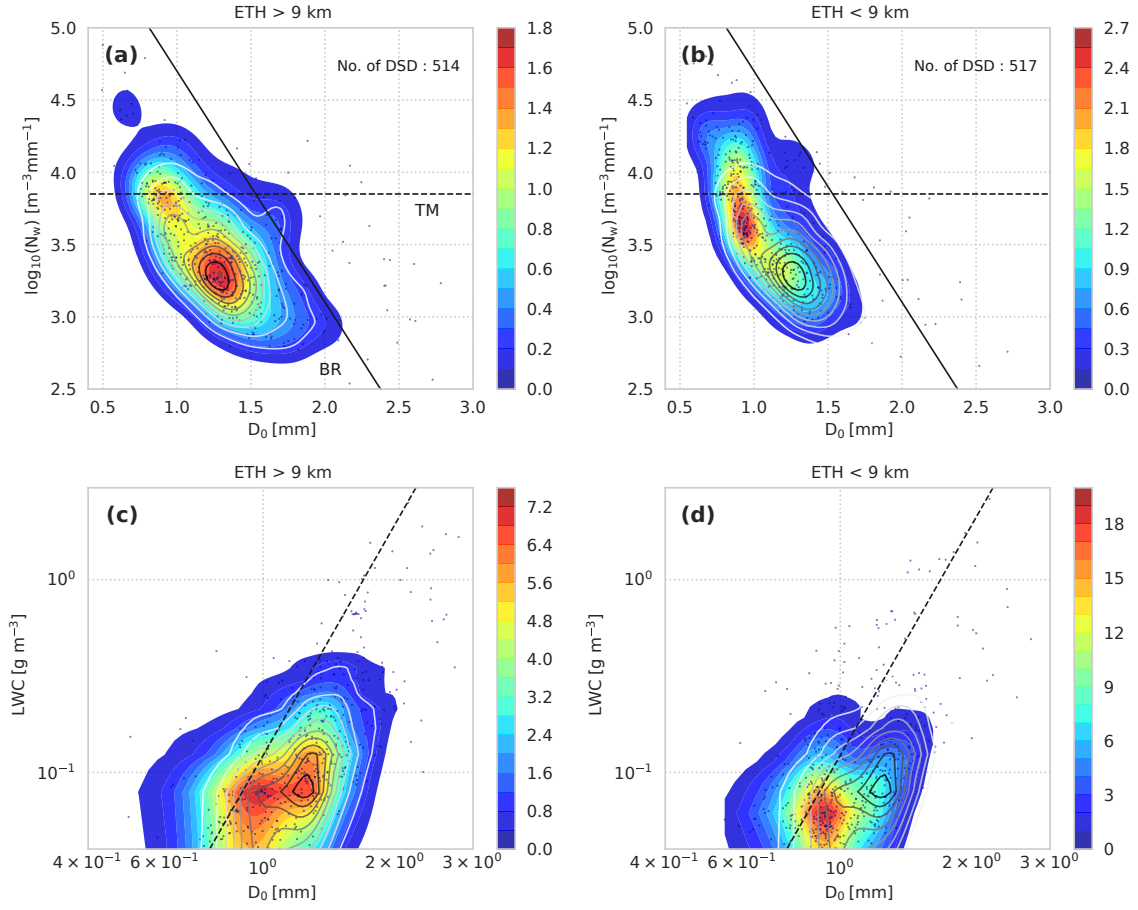


**Figure 11.** Scatter plots of $\log_{10}(N_w)$ versus $D_0$ and LWC versus $D_0$ for RWP-based stratiform DSDs (density on the color scale) and for ETH < 9 km **(a, c)** and ETH > 9 km **(b, d)** DSDs. The overlaid black contours represent the RWP-based classifications for stratiform clouds with bright band precipitating columns.

### 5.2 The Amazon Green Ocean: role of pollution in oceanic signatures?

Overall, the primary shift in precipitation properties for the Amazon coincides with changes in the larger-scale seasonal shifts in thermodynamics and aerosol conditions. In this respect, it is difficult to differentiate relative controls, especially given sampling limits of our Amazon precipitation dataset during the dry season. However, the frequent wet season convective instances (removing the more obvious stratiform contributions) offer some opportunity to test whether we observe any sensitivity to background aerosol conditions and/or other environmental conditions when promoting so-called oceanic DSD properties.

As plotted in Fig. 15, we show the set of convective DSDs observed during the wet season, identifying the relative clean (blues) and polluted (reds) aerosol conditions. The bottom panels illustrate the convective DSDs associated with column ETH < 9 km. Figure 15c and f show a composite median and the 90th and 95th percentile RWP $Z$ profile under the clean and polluted conditions, respectively. For simplicity, polluted regimes in our study combine the more stringent (but, in this dataset, the more frequent) biomass polluted classification with standard polluted designations. During this campaign, a total of 82 clean and 61 polluted events were collected having at least one 5 min convective DSD, with 66 clean events registering an ETH < 9 km DSD and 46 polluted events with a ETH < 9 km DSD.

The mean thermodynamic conditions are sampled from the morning 12:00 UTC radiosondes. For this dataset, clean events record a mean (standard deviation) most unstable convective available potential energy (MUCAPE) of 2124 (1100) $\mathrm{J\,kg^{-1}\,K^{-1}}$, most unstable convective inhibition (MUCIN) of −34 (42) $\mathrm{J\,kg^{-1}\,K^{-1}}$ and average 0–5 km RH of 83 (6) %. Polluted events are slightly more favorable to deeper convection, in recording a higher mean MUCAPE of 2567 (1176) $\mathrm{J\,kg^{-1}\,K^{-1}}$, with a MUCIN of −35 (36) $\mathrm{J\,kg^{-1}\,K^{-1}}$ and RH of 80 (7) %, respectively. Histograms of MUCAPE and MUCIN are shown in the Supplement (Fig. S5). Both clean and polluted events share a similar mean freezing level height at approximately 4.8 km. Over-

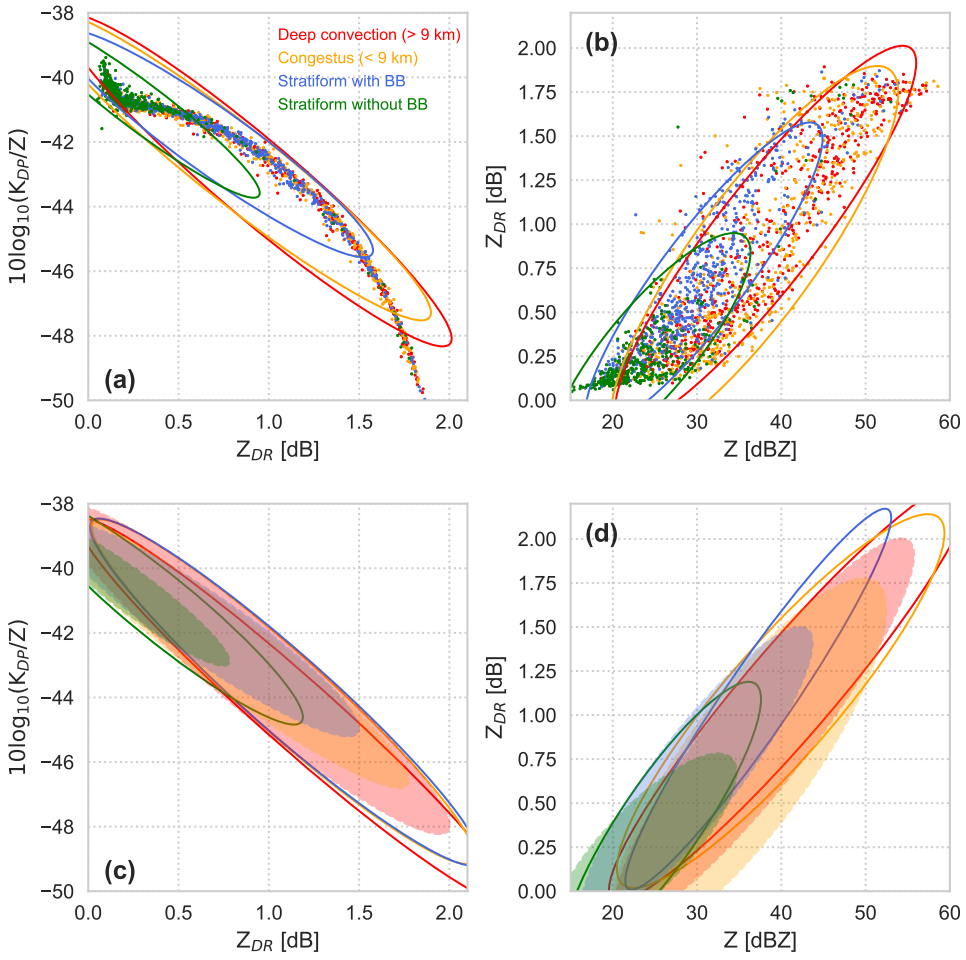


**Figure 12.** Scatter plots of $Z_{DR}$ versus $10\log_{10}(K_{DP}/Z)$ and $Z$ versus $Z_{DR}$ for the various regimes, deep convection, congestus, stratiform with bright band and stratiform without bright band identified by the RWP classifications **(a, b)**. The ellipses convey the two-sigma confidence interval for corresponding regimes. The wet (shaded ellipses) and dry (ellipses) season segregations are presented in **(c, d)**.

all, it is still important to suggest the polluted cases should be more conducive to deeper events based on the available dataset. For the ETH < 9 km panels, mean clean (polluted) environments appear less favorable, with MUCAPE of 1993 (2388) $\mathrm{J\,kg^{-1}\,K^{-1}}$, MUCIN of −36 (−38) $\mathrm{J\,kg^{-1}\,K^{-1}}$ and RH of 83 (81) %. Standard deviations for clean (polluted) values are similar as ETH > 9 km convection.

As indicated in Fig. 15, cleaner regime convective precipitation during the wet season agrees well with oceanic expectations as reported by TM and discussions above. Cumulative polluted regime convective results are less consistent with oceanic expectations, but there is overlap emphasizing DSDs associated with ETH < 9 km columns. Deeper ETH > 9 km polluted convective observations (deeper convection properties) are those most skewed towards the dry season and/or the least oceanic behaviors, including hints of stratiform-type DSD excursions. Inevitably, some DSD contamination could follow from convective-to-stratiform transitional columns in the strongest events as well, for example those featuring sloped updrafts having stronger vertical motions aloft overhanging a stratiform-type downdraft in the column below

Bulk clean and polluted contrasts are potentially visible on the composite $Z$ profiles, with cleaner regime composites demonstrating an increasing $Z$ profile ($Z$ weighted towards increasing contributions from larger drops) towards the surface. One explanation is that these cleaner profiles are more routinely associated with collisional growth process contributions influencing $Z$ profiles over evaporation and/or breakup process influences on radar signatures (e.g., evaporation and/or breakup acting to reduce $Z$, perhaps not observable with available larger drops to RWP wavelengths). These profile behaviors are pronounced for the ETH < 9 km observations that should minimize mixed-phase process influences. In contrast, the polluted regime profiles indicate similar and/or larger $Z$ values aloft to approximately 3.0 km above ground level, with $Z$ profiles peaking and/or decrease in magnitude below these altitudes.

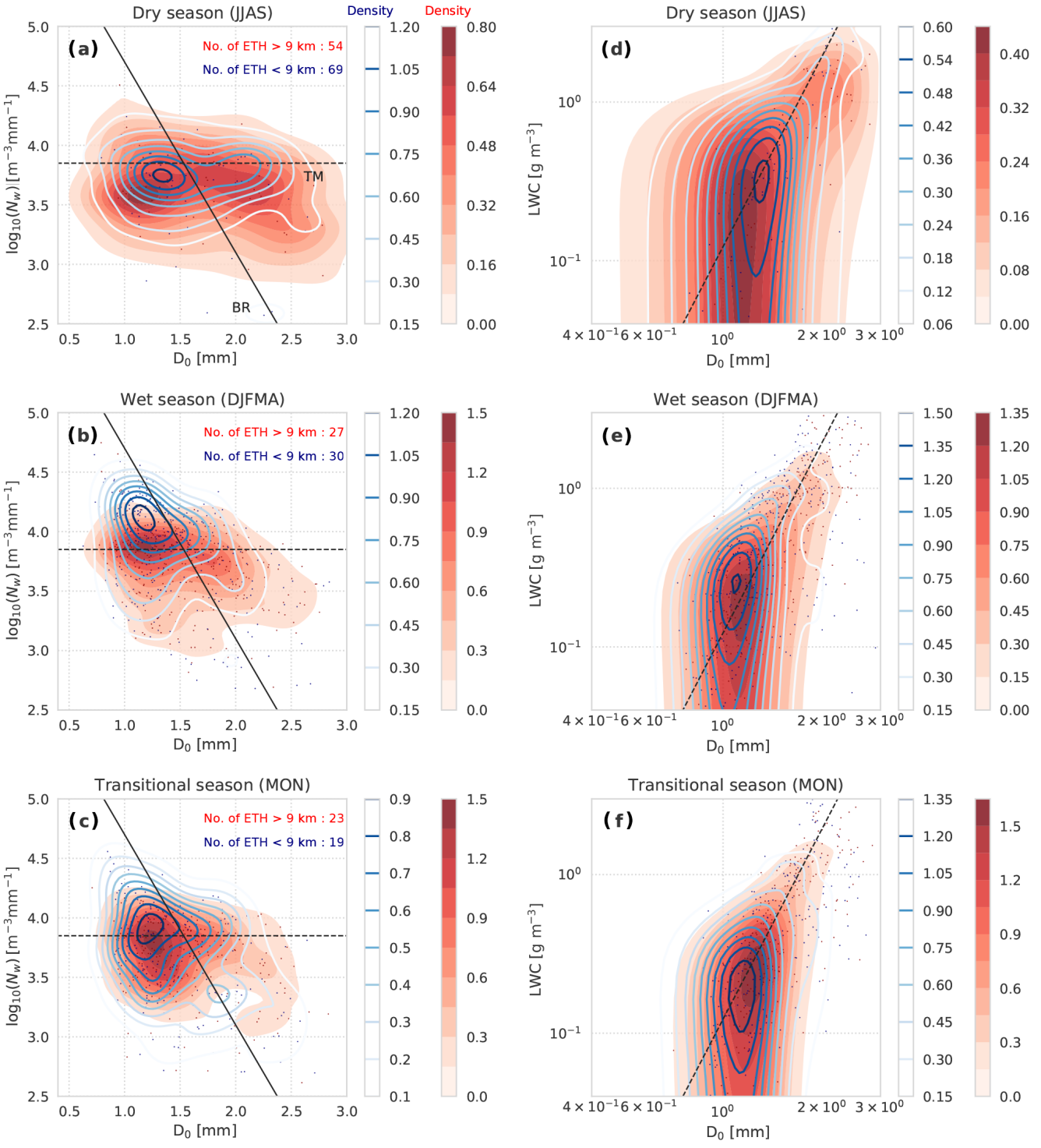


**Figure 13.** Scatter plots of $\log_{10}(N_w)$ versus $D_0$ and LWC versus $D_0$ for RWP-based convective DSDs, for dry **(a, d)**, wet **(b, e)** and transitional **(c, f)** seasons. The contours represent the congestus (ETH < 9 km, blues) and deep (ETH > 9 km, reds) convective DSDs.

One explanation for the polluted profile characteristics in Fig. 15 is that more prominent mixed-phase particle process contributions are acting within these convective columns. Since these polluted events demonstrate more favorable mean thermodynamic conditions that favor stronger convective updrafts, it is possible that an updraft enhancement partially elicits such a transition. A similar response may also be attributed to the proposed role of aerosols in fol-

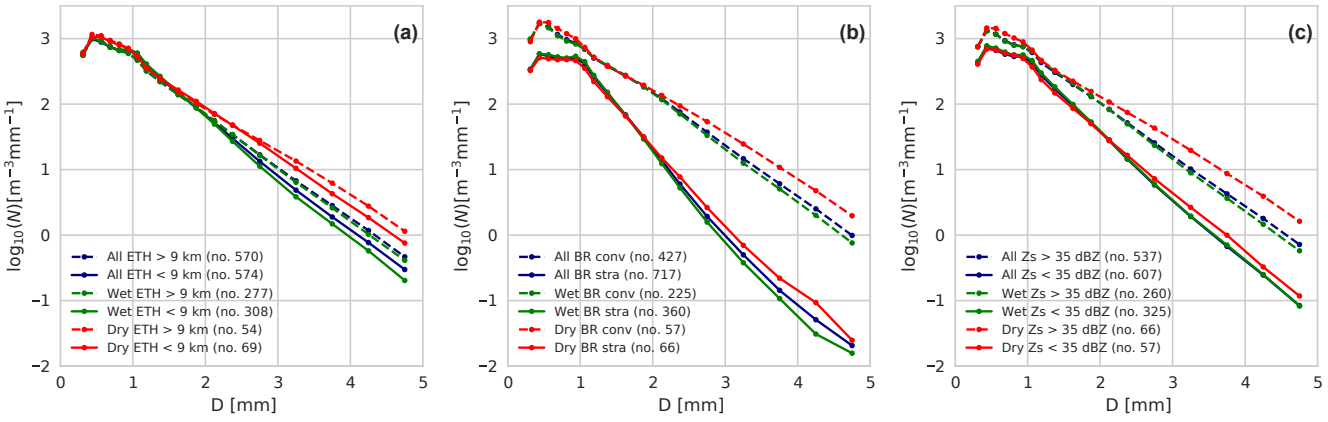


**Figure 14.** Averaged RWP-based convective DSDs for congestus (ETH < 9 km) and deep (ETH > 9 km) DSDs **(a)**, for convective and stratiform DSDs depending on the BR separation **(b)**, and for those having $Z$ (at surface) < 35 dBZ and $Z$ > 35 dBZ **(c)**, for all, dry and wet seasons.

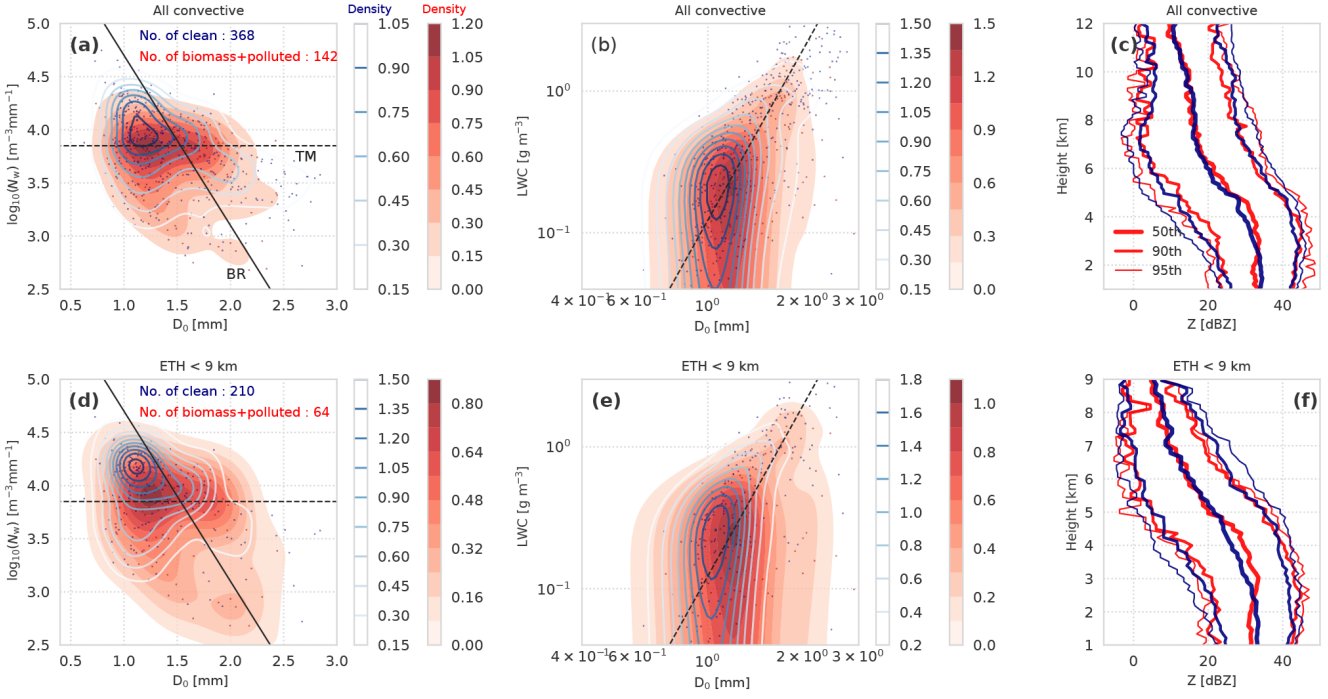


**Figure 15.** Scatter plots of $\log_{10}(N_w)$ versus $D_0$ and LWC versus $D_0$ for RWP-based convective DSDs under the wet season **(a, b)**, as well as for only congestus convective DSDs **(d, e)**, contouring the clean (blues) and polluted (reds) conditions. The corresponding composite median and 90th and 95th percentile RWP $Z$ profile behaviors under the clean (blue) and polluted (red) conditions are shown in **(c)** and **(f)**.

lowing invigoration arguments (e.g., Rosenfeld et al., 2008). For example, recent Amazon aircraft studies as in Braga et al. (2017) indicate changes such as an absence of liquid within growing convective cumulus during polluted conditions, and/or differences in the relative formation and altitudes of ice particles. Regardless of process path, the suggestion is that polluted convective columns would be those that potentially promote added ice depositional growth (resulting in fewer but larger ice particles at the expense of additional liquid). Such physical arguments could help explain the similar or larger $Z$ magnitude aloft (larger ice sizing, offsetting density), coupled with a modest melting enhancement followed by a reduction in $Z$ below 5 km. A reduced number of particles under this scenario would also reduce collisional growth below the freezing level compared to the cleaner profiles. Overall, surface DSD properties in Fig. 15 suggest that cleaner aerosol conditions are associated with enhanced oceanic DSD properties (a.k.a., in agree-

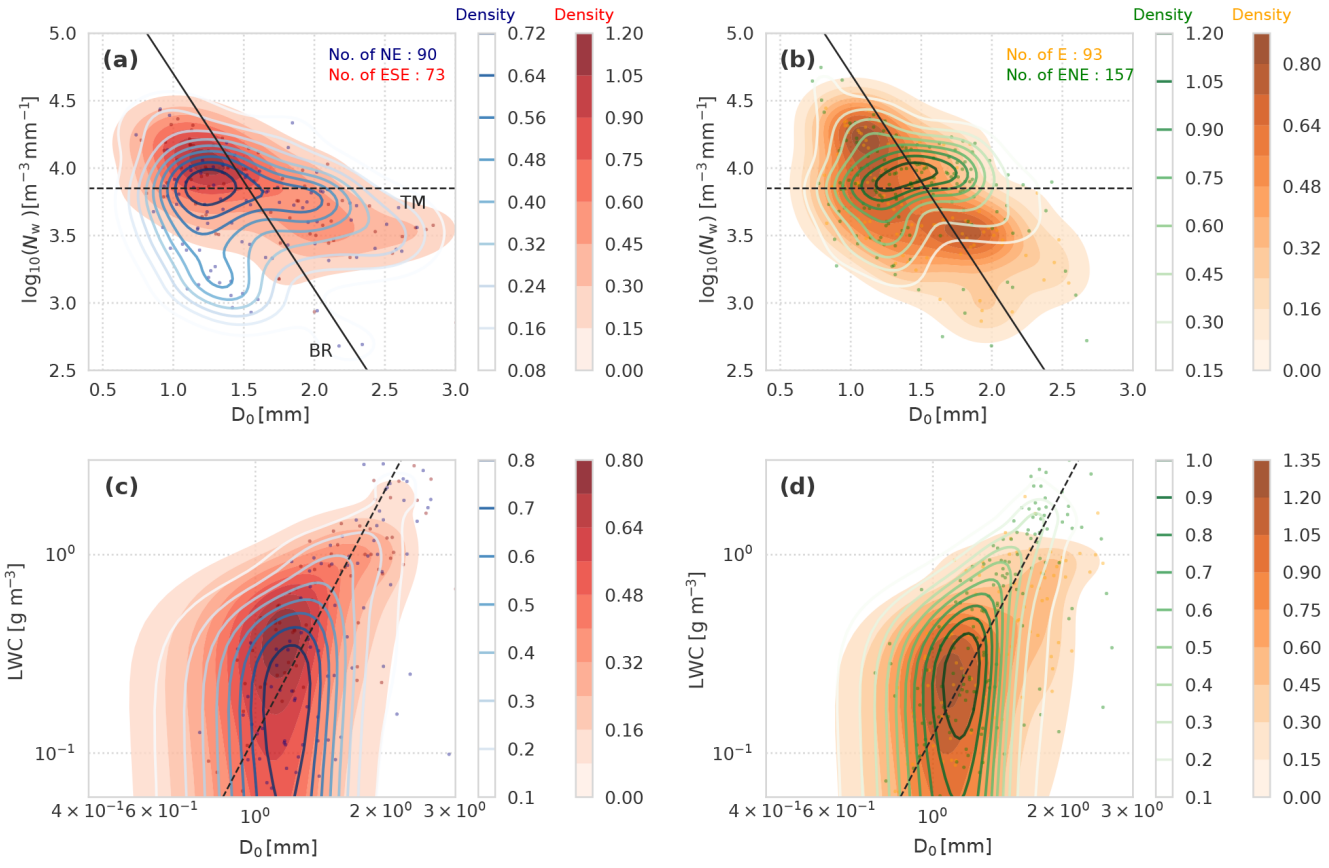


**Figure 16.** Scatter plots of $\log_{10}(N_w)$ versus $D_0$ and LWC versus $D_0$ for wet season DSDs on the ambient wind directions, northeasterly–east-southeasterly (NE – blues; ESE – reds) and east–east-northeast (E – oranges; ENE – greens).

ment with select Green Ocean statements). However, it is nonobvious whether these lesser oceanic conditions (especially within the deeper cores having fewer samples) were the consequence of the aerosol conditions or the shift in the environmental conditions that tracked the change in aerosol.

### 5.3 The Amazon Green Ocean: an alternate explanation

It is useful to determine whether we can better deconvolve environmental influences from aerosol and find those more important to the prevalence of oceanic precipitation characteristics. In Fig. 16, we show wet season DSDs contingent on the ambient wind directions, with relative breakdowns according to the northeasterly–east-southeasterly (NE–ESE) and east–east-northeast (E–ENE) directional pairings. First, the specific NE–ESE and E–ENE pairings were selected for having similar DSD sample sizes. Second, these wind orientations may also be viewed as relevant with respect to the Manaus pollution plume (e.g., E and ENE flows over T3 are arguably the more polluted relative to the Manaus location).

In Fig. 16, we highlight evidence of oceanic-type DSD behaviors according to most wind directions. The fractional polluted versus clean DSD breakdowns along these directions are as follows: NE: 57 % clean and 43 % polluted; ENE: 68 % clean and 32 % polluted; E: 94 % clean and 6 % polluted; ESE: 91 % clean and 9 % polluted. Following Fig. 16, it is found that the larger DSD outlier populations (e.g., convective DSDs found to be least oceanic when compared with TM) are observed for NE and ESE wind directions, and therefore should not be as influenced by a possible Manaus pollution plume. Note, most polluted events sampled during the wet season were attributed to biomass classifications (e.g., local aerosol sources), which may explain NE flows as those most polluted. As expected from discussions above, slightly stronger 12:00 UTC MUCAPE (SD) values are also found along the NE and ENE directions (2207 (1325) and 2131 (934) J kg$^{-1}$ K$^{-1}$, respectively) that are associated with bulk polluted events, while the weakest potential forcing conditions are found with the ESE and E flows (2089 (1241) and 1766 (1035) J kg$^{-1}$ K$^{-1}$, respectively). Nevertheless, these local thermodynamic controls associated with wind direction are far less pronounced than previous polluted–clean contrasts. The histograms for MUCAPE and MUCIN as a function of wind direction are found in the Supplement (Fig. S6).

The DSDs observed along NE wind flows reflect the least oceanic characteristics in this dataset, favoring low $N_w$–$D_0$ pairings typical of dry season convection (also carrying $Z$ profiles similar to in Fig. 15, not shown). Again, these NE flows reflect the most polluted wind components, and directions associated with the larger mean convective forcing parameters associated with higher values towards the tail of the MUCAPE distributions (Fig. S6 in the Supplement). In that regard, a reduced presence for oceanic-type DSDs was not unexpected. However, the pronounced absence of oceanic DSD characteristics along NE flows is far more noteworthy than when contrasted to previous clean–polluted criteria, and not immediately in line with mean thermodynamic values. From event inspection, most nonoceanic DSD characteristics were associated with isolated, deeper convective cell events, or widespread convective events still demonstrating deeper cloud ETH. Widespread, shallower convective events or organized shallow systems (possible Amazon warm-rain dominant systems as observed over oceans; e.g., Chen and Liu, 2015) were not favored, compared with other wind components. Again, this change may be attributed to the frequency of higher MUCAPE at the tail of the NE distribution (Fig. S6 in the Supplement).

Additional outlier DSD populations (including several events having numerous oceanic DSD properties) are observed according to ESE wind directions (relatively clean). These DSDs reflect the presence of deeper convective DSDs (to the right of the BR separation line) that exhibit high concentrations of larger relative drop sizes. These regions, although not typical of TM oceanic examples, are also not consistent with Amazon dry season characteristics (having a relatively higher triplet of LWC, $D_0$ and $N_w$). As in NE flow examples, the basic radiosonde parameter checks and aerosol forcing controls associated with these events are in line with the other wind components. However, histograms in Fig. S6 in the Supplement do show a similar enhancement for the frequency of higher MUCAPE values towards the tail of the distribution.

As far as potential explanations for why these outliers cluster according to particular wind directions compared to other environmental factors, it is important to note that while Amazon convection timing follows a well-established diurnal cycle over T3, 12:00 UTC radiosondes and associated parameters (those typically closest to earlier convective initiation) may not be completely representative of the important larger-scale conditions (e.g., South Atlantic Convergence Zone (SACZ) positioning, influences on the Amazon basin during the wet season; Carvalho et al., 2004). For one example, wet season sea-breeze intrusion and associated statistical cloud enhancements (as determined by satellite) into the Amazon basin orient tangential to a NE–SW axis over the T3. This sea-breeze front passage is in phase with this T3 diurnal precipitation cycle (e.g., see composite convective evolution as in Burleyson et al., 2016). It is possible that similar forms of dynamical or moisture enhancements, for example SACZ drivers of frontal intrusions, as well as river breeze influences (e.g., Tanaka et al., 2014; Burleyson et al., 2016), would not be completely captured by our morning radiosonde observations (given their timing). However, these larger-scale features may promote enhancements sufficient to spark possible changes in cloud initiation and subsequent precipitation properties.

From inspection of events according to wind directions, ESE events tended to emphasize widespread organized convective events exhibiting copious rainfall along a NE–SW orientation (with winds flowing from ESE preceding those lines), having a shallower ETH < 9 km. Timing for these events was near or just following the afternoon diurnal maximum (18:00–20:00 UTC). One suggestion is that the oceanic DSDs tended to be associated with these shallower but widespread convective events initiated or enhanced by sea breeze, Kelvin waves or other influences. As the conditions are also clean, this is also consistent with shallower, oceanic forms of organized convection. These combined concepts and possible SACZ influences on these events are the subject of ongoing research. In contrast, NE events most often reflected deeper events (ETH > 9 km) with less evidence for forms of NE–SW linear or shallow cloud organization for animations of the widespread events. Deeper clouds would be consistent with pollution arguments as above, but these breakdowns speak to the complexities of these studies.

## 6 Conclusions

This study summarizes Amazon precipitation properties collected during the unique, multi-year GoAmazon2014/5 campaign. Emphasis was placed on cumulative campaign precipitation properties and relationships that may benefit potential hydrological applications and radar-based precipitation data product development, as well as connections relevant to future Amazon convective model evaluation. The study also explored Amazon precipitation properties from the perspective of possible Green Ocean convective characteristics, including possible thermodynamic and aerosol forcing influences that may be influential to observations of oceanic-like precipitation.

Amazon rainfall and radar self-consistency relationships demonstrate tropical characteristics as compared to continental SGP references, associated with radar quantities (in both convective and stratiform contexts) that sample higher relative concentrations of smaller drops. Typically, this indicates a reduced role for convective mixed-phase and/or graupel growth, as well as stratiform aggregation processes in the Amazon. These tropical precipitation characteristics are more pronounced within the wet seasons than dry season events, with dry season events favoring the presence of larger drop sizes as a suggested consequence of stronger event updrafts under more favorable thermodynamic conditions. Although it is difficult to differentiate wet–dry regimes exclu-

sively using radar quantities, our analysis suggests $Z$, $Z_{DR}$ and $K_{DP}$ would exhibit larger values within dry season events and deeper convective cores therein.

Coupled RWP and disdrometer Amazon T3 precipitation breakdowns confirm the overall findings of previous ARM campaign BR and TM studies on tropical convective to oceanic-type cloud and precipitation breakdowns. Amazon precipitation is varied and often found to straddle maritime continental behaviors as seen in previous studies, with DSD excursions into the more oceanic examples presented from ARM Manus and Gan deployments. As before, the separations between wet and dry seasons are pronounced, with most oceanic DSD conditions observed during the wet season. The strongest convective behaviors, as well as events having a marked absence of stratiform precipitation, are observed during the Amazon dry season.

Considering deeper versus congestus properties, Amazon congestus clouds are attributed to the more oceanic precipitation behaviors found in our dataset. When exploring Green Ocean themes, our analysis was not able to demonstrate that either aerosol conditions or enhanced local convective forcing parameters were strongly associated with the presence/absence of an oceanic character of the congestus and deeper precipitation. Rather, the more pronounced separation was found when segregating by wind direction, which may reflect that our initial options for thermodynamic or aerosol controls are all unable to deconvolve a more subtle change important to an enhanced DSD signature. However, there is evidence to support that aerosol or other early morning forcing factors within the wet season are not significantly different to promote these differences. Rather, episodic to frequent larger-scale Amazon basin (e.g., SACZ, sea breeze) or river forcing controls and associated enhancements may require future investigation to determine their importance to the apparent oceanic nature of the clouds and eventual precipitation. Other factors including the possible role of aerosol sizing (e.g., Fan et al., 2018) on updraft and precipitation enhancements for Amazon convection are also a topic of future consideration.

*Data availability.* All ARM datasets used for this study can be downloaded at http://www.arm.gov and are associated with several "value added" product streams. PyDSD is available at https://doi.org/105281/zenodo.9991.

**The Supplement related to this article is available online at https://doi.org/10.5194/acp-18-9121-2018-supplement.**

*Author contributions.* DW and SEG designed and performed research; MJB, RT and LATM performed data collection and preliminary analysis; JH performed disdrometer processing routines; DW, SEG, ZF and LATM wrote the paper

*Competing interests.* The authors declare that they have no conflict of interest.

*Acknowledgements.* This paper has been authored by employees of Brookhaven Science Associates, LLC, under contract no DE-SC0012704 with the U.S. Department of Energy (DOE). The publisher by accepting the paper for publication acknowledges that the United States Government retains a nonexclusive, paid-up, irrevocable, worldwide license to publish or reproduce the published form of this paper, or allow others to do so, for United States Government purposes. Joseph Hardin and Zhe Feng at the Pacific Northwest National Laboratory (PNNL) are supported by the Climate Model Development and Validation activity funded by the Office of Biological and Environmental Research in the U.S. Department of Energy, Office of Science and also acknowledge the Atmospheric Radiation Measurement (ARM) Climate Research Facility, a user facility of the U.S. DOE, Office of Science, sponsored by the Office of Biological and Environmental Research, and support from the ASR program of that office.

Edited by: Timothy Garrett
Reviewed by: two anonymous referees

## References

Ackerman, T. P. and Stokes, G. M.: The Atmospheric Radiation Measurement Program, Phys. Today, 56, 38–44, https://doi.org/10.1063/1.1554135, 2003.

Bartholomew, M.: ARM's Handbook for the Parsivel2 Laser Disdrometer, Tech. rep., US DOE, Office of Science, Office of Biological and Environmental Research, 2014.

Braga, R. C., Rosenfeld, D., Weigel, R., Jurkat, T., Andreae, M. O., Wendisch, M., Pöschl, U., Voigt, C., Mahnke, C., Borrmann, S., Albrecht, R. I., Molleker, S., Vila, D. A., Machado, L. A. T., and Grulich, L.: Further evidence for CCN aerosol concentrations determining the height of warm rain and ice initiation in convective clouds over the Amazon basin, Atmos. Chem. Phys., 17, 14433–14456, https://doi.org/10.5194/acp-17-14433-2017, 2017.

Bringi, V. N., Huang, G.-J., Chandrasekar, V., and Gorgucci, E.: A Methodology for Estimating the Parameters of a Gamma Raindrop Size Distribution Model from Polarimetric Radar Data: Application to a Squall-Line Event from the TRMM/Brazil Campaign, J. Atmos. Ocean. Technol., 19, 633–645, https://doi.org/10.1175/1520-0426(2002)019<0633:AMFETP>2.0.CO;2, 2002.

Bringi, V. N., Chandrasekar, V., Hubbert, J., Gorgucci, E., Randeu, W. L., and Schoenhuber, M.: Raindrop Size Distribution in Different Climatic Regimes from Disdrometer and Dual-Polarized Radar Analysis, J. Atmos. Sci., 60, 354–365, https://doi.org/10.1175/1520-0469(2003)060<0354:RSDIDC>2.0.CO;2, 2003.

Bringi, V. N., Williams, C. R., Thurai, M., and May, P. T.: Using Dual-Polarized Radar and Dual-Frequency Profiler for DSD Characterization: A Case Study from Darwin, Australia, J. Atmos. Ocean. Technol., 26, 2107–2122, https://doi.org/10.1175/2009JTECHA1258.1, 2009.

Burleyson, C. D., Feng, Z., Hagos, S. M., Fast, J., Machado, L. A. T., and Martin, S. T.: Spatial Variability of the Background Diurnal Cycle of Deep Convection around the GoAmazon2014/5 Field Campaign Sites, J. Appl. Meteorol. Climatol., 55, 1579–1598, https://doi.org/10.1175/JAMC-D-15-0229.1, 2016.

Cao, Q. and Zhang, G.: Errors in Estimating Raindrop Size Distribution Parameters Employing Disdrometer and Simulated Raindrop Spectra, J. Appl. Meteorol. Climatol., 48, 406–425, https://doi.org/10.1175/2008JAMC2026.1, 2009.

Carvalho, L. M. V., Jones, C., and Liebmann, B.: The South Atlantic Convergence Zone: Intensity, Form, Persistence, and Relationships with Intraseasonal to Interannual Activity and Extreme Rainfall, J. Climate, 17, 88–108, 2004.

Cecchini, M. A., Machado, L. A. T., Comstock, J. M., Mei, F., Wang, J., Fan, J., Tomlinson, J. M., Schmid, B., Albrecht, R., Martin, S. T., and Artaxo, P.: Impacts of the Manaus pollution plume on the microphysical properties of Amazonian warm-phase clouds in the wet season, Atmos. Chem. Phys., 16, 7029–7041, https://doi.org/10.5194/acp-16-7029-2016, 2016.

Chen, B. and Liu, C.: Warm organized rain systems over the topical eastern Pacific, J. Climate, 29, 3403–3422, https://doi.org/10.1175/JCLI-D-15-0177.1, 2015.

Cifelli, R., Carey, L., Petersen, W. A., and Rutledge, S. A.: An Ensemble Study of Wet Season Convection in Southwest Amazonia: Kinematics and Implications for Diabatic Heating, J. Climate, 17, 4692–4707, https://doi.org/10.1175/JCLI-3236.1, 2004.

Coulter, R., Martin, T., and Muradyan, P.: Updated hourly, Radar Wind Profiler (1290RWPPRECIPMOM), Tech. rep., Atmospheric Radiation Measurement (ARM) Climate Research Facility Data Archive: Oak Ridge, Tenn., 2009.

Del Genio, A. D.: Representing the Sensitivity of Convective Cloud Systems to Tropospheric Humidity in General Circulation Models, Surv. Geophys., 33, 637–656, https://doi.org/10.1007/s10712-011-9148-9, 2012.

Dolan, B., Rutledge, S. A., Lim, S., Chandrasekar, V., and Thurai, M.: A Robust C-Band Hydrometeor Identification Algorithm and Application to a Long-Term Polarimetric Radar Dataset, J. Appl. Meteorol. Climatol., 52, 2162–2186, https://doi.org/10.1175/JAMC-D-12-0275.1, 2013.

Dolan, B., Fuchs, B., Rutledge, S. A., Barnes, E. A., and Thompson, E. J.: Primary Modes of Global Drop Size Distributions, J. Atmos. Sci., 75, 1453–1476, https://doi.org/10.1175/JAS-D-17-0242.1, 2018.

Donner, L. J., O'Brien, T. A., Rieger, D., Vogel, B., and Cooke, W. F.: Are atmospheric updrafts a key to unlocking climate forcing and sensitivity?, Atmos. Chem. Phys., 16, 12983–12992, https://doi.org/10.5194/acp-16-12983-2016, 2016.

Duchon, C. E. and Essenberg, G. R.: Comparative rainfall observations from pit and aboveground rain gauges with and without wind shields, Water Resour. Res., 37, 3253–3263, https://doi.org/10.1029/2001WR000541, 2001.

Fabry, F. and Zawadzki, I.: Long-Term Radar Observations of the Melting Layer of Precipitation and Their Interpretation, J. Atmos. Sci., 52, 838–851, https://doi.org/10.1175/1520-0469(1995)052<0838:LTROOT>2.0.CO;2, 1995.

Fan, J., Rosenfeld, D., Zhang, Y., Giangrande, S. E., Li, Z., Machado, L. A. T., Martin, S. T., Yang, Y., Wang, J., Artaxo, P., Barbosa, H. M. J., Braga, R. C., Comstock, J. M., Feng, Z., Gao, W., Gomes, H. B., Mei, F., Pöhlker, C., Pöhlker, M. L., Pöschl, U., and de Souza, R. A. F.: Substantial convection and precipitation enhancements by ultrafine aerosol particles, Science, 359, 411–418, https://doi.org/10.1126/science.aan8461, 2018.

Geerts, B. and Dawei, Y.: Classification and Characterization of Tropical Precipitation Based on High-Resolution Airborne Vertical Incidence Radar. Part I: Classification, J. Appl. Meteorol., 43, 1554–1566, 2004.

Giangrande, S. E., Collis, S., Straka, J., Protat, A., Williams, C., and Krueger, S.: A Summary of Convective-Core Vertical Velocity Properties Using ARM UHF Wind Profilers in Oklahoma, J. Appl. Meteorol. Climatol., 52, 2278–2295, https://doi.org/10.1175/JAMC-D-12-0185.1, 2013.

Giangrande, S. E., Bartholomew, M. J., Pope, M., Collis, S., and Jensen, M. P.: A Summary of Precipitation Characteristics from the 2006–11 Northern Australian Wet Seasons as Revealed by ARM Disdrometer Research Facilities (Darwin, Australia), J. Appl. Meteorol. Climatol., 53, 1213–1231, https://doi.org/10.1175/JAMC-D-13-0222.1, 2014a.

Giangrande, S. E., Collis, S., Theisen, A. K., and Tokay, A.: Precipitation Estimation from the ARM Distributed Radar Network during the MC3E Campaign, J. Appl. Meteorol. Climatol., 53, 2130–2147, https://doi.org/10.1175/JAMC-D-13-0321.1, 2014b.

Giangrande, S. E., Toto, T., Bansemer, A., Kumjian, M. R., Mishra, S., and Ryzhkov, A. V.: Insights into riming and aggregation processes as revealed by aircraft, radar, and disdrometer observations for a 27 April 2011 widespread precipitation event, J. Geophys. Res.-Atmos., 121, 5846–5863, https://doi.org/10.1002/2015JD024537, 2016a.

Giangrande, S. E., Toto, T., Jensen, M. P., Bartholomew, M. J., Feng, Z., Protat, A., Williams, C. R., Schumacher, C., and Machado, L.: Convective cloud vertical velocity and mass-flux characteristics from radar wind profiler observations during GoAmazon2014/5, J. Geophys. Res.-Atmos., 121, 12891–12913, https://doi.org/10.1002/2016JD025303, 2016b.

Giangrande, S. E., Feng, Z., Jensen, M. P., Comstock, J. M., Johnson, K. L., Toto, T., Wang, M., Burleyson, C., Bharadwaj, N., Mei, F., Machado, L. A. T., Manzi, A. O., Xie, S., Tang, S., Silva Dias, M. A. F., de Souza, R. A. F., Schumacher, C., and Martin, S. T.: Cloud characteristics, thermodynamic controls and radiative impacts during the Observations and Modeling of the Green Ocean Amazon (GoAmazon2014/5) experiment, Atmos. Chem. Phys., 17, 14519–14541, https://doi.org/10.5194/acp-17-14519-2017, 2017.

Hardin, J.: PyDisdrometer Version v1.0, https://github.com/josephhardinee/PyDSD (last access: 27 June 2018), 2014.

Hardin, J. and Guy, N.: PyDSD, https://doi.org/oi.org/10.5281/zenodo.9991, 2017.

Hou, A. Y., Kakar, R. K., Neeck, S., Azarbarzin, A. A., Kummerow, C. D., Kojima, M., Oki, R., Nakamura, K., and Iguchi, T.: The Global Precipitation Measurement Mission, B. Am. Meteor. Soc., 95, 701–722, https://doi.org/10.1175/BAMS-D-13-00164.1, 2014.

Houze, R. A.: Stratiform Precipitation in Regions of Convection: A Meteorological Paradox?, B. Am. Meteor. Soc., 78, 2179–2196, https://doi.org/10.1175/1520-0477(1997)078<2179:SPIROC>2.0.CO;2, 1997.

Jensen, M. P. and Del Genio, A. D.: Factors Limiting Convective Cloud-Top Height at the ARM Nauru Island

Climate Research Facility, J. Climate, 19, 2105–2117, https://doi.org/10.1175/JCLI3722.1, 2006.

Johnson, R. H., Rickenbach, T. M., Rutledge, S. A., Ciesielski, P. E., and Schubert, W. H.: Trimodal Characteristics of Tropical Convection, J. Climate, 12, 2397–2418, https://doi.org/10.1175/1520-0442(1999)012<2397:TCOTC>2.0.CO;2, 1999.

Klein, S. and Genio, A. D.: ARM's Support for GCM Improvement: A White Paper, Tech. rep., U.S. Department of Energy, Washington, D.C., 2006.

Lang, S., Tao, W.-K., Simpson, J., and Ferrier, B.: Modeling of Convective–Stratiform Precipitation Processes: Sensitivity to Partitioning Methods, J. Appl. Meteorol., 42, 505–527, https://doi.org/10.1175/1520-0450(2003)042<0505:MOCSPP>2.0.CO;2, 2003.

Lee, C. K., Lee, G. W., Zawadzki, I., and Kim, K.-E.: A Preliminary Analysis of Spatial Variability of Raindrop Size Distributions during Stratiform Rain Events, J. Appl. Meteorol. Climatol., 48, 270–283, https://doi.org/10.1175/2008JAMC1877.1, 2009.

Li, W. and Fu, R.: Transition of the Large-Scale Atmospheric and Land Surface Conditions from the Dry to the Wet Season over Amazonia as Diagnosed by the ECMWF Re-Analysis, J. Climate, 17, 2637–2651, https://doi.org/10.1175/1520-0442(2004)017<2637:TOTLAA>2.0.CO;2, 2004.

Löffler-Mang, M. and Joss, J.: An Optical Disdrometer for Measuring Size and Velocity of Hydrometeors, J. Atmos. Ocean. Technol., 17, 130–139, https://doi.org/10.1175/1520-0426(2000)017<0130:AODFMS>2.0.CO;2, 2000.

Long, C. N., Mather, J. H., and Ackerman, T. P.: The ARM Tropical Western Pacific (TWP) Sites, Meteorol. Monogr., 57, 7.1–7.14, https://doi.org/10.1175/AMSMONOGRAPHS-D-15-0024.1, 2016.

Machado, L. A. T., Laurent, H., Dessay, N., and Miranda, I.: Seasonal and diurnal variability of convection over the Amazonia: A comparison of different vegetation types and large scale forcing, Theor. Appl. Climatol., 78, 61–77, https://doi.org/10.1007/s00704-004-0044-9, 2004.

Martin, S. T., Artaxo, P., Machado, L. A. T., Manzi, A. O., Souza, R. A. F., Schumacher, C., Wang, J., Andreae, M. O., Barbosa, H. M. J., Fan, J., Fisch, G., Goldstein, A. H., Guenther, A., Jimenez, J. L., Pöschl, U., Silva Dias, M. A., Smith, J. N., and Wendisch, M.: Introduction: Observations and Modeling of the Green Ocean Amazon (GoAmazon2014/5), Atmos. Chem. Phys., 16, 4785–4797, https://doi.org/10.5194/acp-16-4785-2016, 2016.

Martin, S. T., Artaxo, P., Machado, L., Manzi, A. O., Souza, R. A. F., Schumacher, C., Wang, J., Biscaro, T., Brito, J., Calheiros, A., Jardine, K., Medeiros, A., Portela, B., de Sá, S. S., Adachi, K., Aiken, A. C., Albrecht, R., Alexander, L., Andreae, M. O., Barbosa, H. M. J., Buseck, P., Chand, D., Comstock, J. M., Day, D. A., Dubey, M., Fan, J., Fast, J., Fisch, G., Fortner, E., Giangrande, S., Gilles, M., Goldstein, A. H., Guenther, A., Hubbe, J., Jensen, M., Jimenez, J. L., Keutsch, F. N., Kim, S., Kuang, C., Laskin, A., McKinney, K., Mei, F., Miller, M., Nascimento, R., Pauliquevis, T., Pekour, M., Peres, J., Petäjä, T., Pöhlker, C., Pöschl, U., Rizzo, L., Schmid, B., Shilling, J. E., Dias, M. A. S., Smith, J. N., Tomlinson, J. M., Tóta, J., and Wendisch, M.: The Green Ocean Amazon Experiment (GoAmazon2014/5) Observes Pollution Affecting Gases, Aerosols, Clouds, and Rainfall over the Rain Forest, B. Am. Meteor. Soc., 98, 981–997, https://doi.org/10.1175/BAMS-D-15-00221.1, 2017.

Mather, J. H. and Voyles, J. W.: The Arm Climate Research Facility: A Review of Structure and Capabilities, B. Am. Meteor. Soc., 94, 377–392, https://doi.org/10.1175/BAMS-D-11-00218.1, 2013.

May, P. T. and Ballinger, A.: The Statistical Characteristics of Convective Cells in a Monsoon Regime (Darwin, Northern Australia), Mon. Weather Rev., 135, 82–92, https://doi.org/10.1175/MWR3273.1, 2007.

Miller, M. A., Nitschke, K., Ackerman, T. P., Ferrell, W., Hickmon, N., and Ivey, M.: The Atmospheric Radiation Measurement Mobile Facility, The Atmospheric Radiation Measurement (ARM) Program: AMS Monograph, The first 20 years of ARM, Am. Meteorol. Soc., https://doi.org/10.1175/AMSMONOGRAPHS-D-15-0051.1, 2016.

Mishchenko, M., Travis, L., and Mackowski, D.: T-matrix computations of light scattering by nonspherical particles: A review, J. Quant. Spectrosc. Radiat. Transf., 55, 535–575, https://doi.org/10.1016/0022-4073(96)00002-7, 1996.

Misra, V.: Coupled Air, Sea, and Land Interactions of the South American Monsoon, J. Climate, 21, 6389–6403, https://doi.org/10.1175/2008JCLI2497.1, 2008.

Park, S.-G., Kim, H.-L., Ham, Y.-W., and Jung, S.-H.: Comparative Evaluation of the OTT PARSIVEL2 Using a Collocated Two-Dimensional Video Disdrometer, J. Atmos. Ocean. Technol., 34, 2059–2082, https://doi.org/10.1175/JTECH-D-16-0256.1, 2017.

Roberts, G. C., O., A. M., Jingchuan, Z., and Paulo, A.: Cloud condensation nuclei in the Amazon Basin: "marine" conditions over a continent?, Geophys. Res. Lett., 28, 2807–2810, https://doi.org/10.1029/2000GL012585, 2001.

Rosenfeld, D., Lohmann, U., Raga, G. B., O'Dowd, C. D., Kulmala, M., Fuzzi, S., Reissell, A., and Andreae, M. O.: Flood or Drought: How Do Aerosols Affect Precipitation?, Science, 321, 1309–1313, https://doi.org/10.1126/science.1160606, 2008.

Ryzhkov, A., Diederich, M., Zhang, P., and Simmer, C.: Potential Utilization of Specific Attenuation for Rainfall Estimation, Mitigation of Partial Beam Blockage, and Radar Networking, J. Atmos. Ocean. Technol., 31, 599–619, https://doi.org/10.1175/JTECH-D-13-00038.1, 2014.

Ryzhkov, A. V., Giangrande, S. E., Melnikov, V. M., and Schuur, T. J.: Calibration Issues of Dual-Polarization Radar Measurements, J. Atmos. Ocean. Technol., 22, 1138–1155, https://doi.org/10.1175/JTECH1772.1, 2005.

Scarchilli, G., Gorgucci, E., Chandrasekar, V., and Dobaie, A.: Self-consistency of polarization diversity measurement of rainfall, IEEE T. Geosci. Remote Sens., 34, 22–26, 1996.

Schiro, K. A.: Thermodynamic Controls on Deep Convection in the Tropics: Observations and Applications to Modeling, dissertation, University of California, 2017.

Schumacher, C., Stevenson, S. N., and Williams, C. R.: Vertical motions of the tropical convective cloud spectrum over Darwin, Australia., Q. J. Roy. Meteorol. Soc., 141, 2277–2288, 2015.

Smith, P. L., Kliche, D. V., and Johnson, R. W.: The Bias and Error in Moment Estimators for Parameters of Drop Size Distribution Functions: Sampling from Gamma Distributions, J. Appl. Meteorol. Climatol., 48, 2118–2126, https://doi.org/10.1175/2009JAMC2114.1, 2009.

Steiner, M., R. A. Houze, J., and Yuter, S. E.: Climatological characterization of three-dimensional storm structure from operational

radar and rain gauge data, J. Appl. Meteorol., 34, 1978–2007, 1995.

Steiner, M., Smith, J. A., and Uijlenhoet, R.: A Microphysical Interpretation of Radar Reflectivity – Rain Rate Relationships, J. Atmos. Sci., 61, 1114–1131, https://doi.org/10.1175/1520-0469(2004)061<1114:AMIORR>2.0.CO;2, 2004.

Tanaka, L. M. D. S., Satyamurty, P., and Machado, L. A. T.: Diurnalcvariation of precipitation in central Amazon basin, Int J. Climatol., 34, 3574–3584, 2014.

Testud, J., Oury, S., Black, R. A., Amayenc, P., and Dou, X.: The Concept of "Normalized" Distribution to Describe Raindrop Spectra: A Tool for Cloud Physics and Cloud Remote Sensing, J. Appl. Meteorol., 40, 1118–1140, https://doi.org/10.1175/1520-0450(2001)040<1118:TCONDT>2.0.CO;2, 2001.

Thalman, R., de Sá, S. S., Palm, B. B., Barbosa, H. M. J., Pöhlker, M. L., Alexander, M. L., Brito, J., Carbone, S., Castillo, P., Day, D. A., Kuang, C., Manzi, A., Ng, N. L., Sedlacek III, A. J., Souza, R., Springston, S., Watson, T., Pöhlker, C., Pöschl, U., Andreae, M. O., Artaxo, P., Jimenez, J. L., Martin, S. T., and Wang, J.: CCN activity and organic hygroscopicity of aerosols downwind of an urban region in central Amazonia: seasonal and diel variations and impact of anthropogenic emissions, Atmos. Chem. Phys., 17, 11 779–11 801, https://doi.org/10.5194/acp-17-11779-2017, 2017.

Thompson, E. J., Rutledge, S. A., Dolan, B., and Thurai, M.: Drop Size Distributions and Radar Observations of Convective and Stratiform Rain over the Equatorial Indian and West Pacific Oceans, J. Atmos. Sci., 72, 4091–4125, https://doi.org/10.1175/JAS-D-14-0206.1, 2015.

Thurai, M., Huang, G. J., Bringi, V. N., Randeu, W. L., and Schönhuber, M.: Drop Shapes, Model Comparisons, and Calculations of Polarimetric Radar Parameters in Rain, J. Atmos. Ocean. Technol., 24, 1019–1032, https://doi.org/10.1175/JTECH2051.1, 2007.

Thurai, M., Gatlin, P., Bringi, V. N., Petersen, W., Kennedy, P., Notaros, B., and Carey, L.: Toward completing the raindrops size spectrum: Case studies involving 2D-video disdrometer, droplet spectrometer, and polarimetric radar measurements, J. Appl. Meteor. Climatol., 56, 877–896, 2017.

Tokay, A. and Short, D. A.: Evidence from Tropical Raindrop Spectra of the Origin of Rain from Stratiform versus Convective Clouds, J. Appl. Meteorol., 35, 355–371, https://doi.org/10.1175/1520-0450(1996)035<0355:EFTRSO>2.0.CO;2, 1996.

Tokay, A., Petersen, W. A., Gatlin, P., and Wingo, M.: Comparison of Raindrop Size Distribution Measurements by Collocated Disdrometers, J. Atmos. Ocean. Technol., 30, 1672–1690, https://doi.org/10.1175/JTECH-D-12-00163.1, 2013.

Tokay, A., Wolff, D. B., and Petersen, W. A.: Evaluation of the New Version of the Laser-Optical Disdrometer, OTT Parsivel2, J. Atmos. Ocean. Technol., 31, 1276–1288, https://doi.org/10.1175/JTECH-D-13-00174.1, 2014.

Tridon, F., Battaglia, A., Kollias, P., Luke, E., and Williams, C. R.: Signal postprocessing and reflectivity calibration of the Atmospheric Radiation Measurement 915-MHz wind profilers, J. Atmos. Ocean. Technol., 30, 1038–1054, 2013.

Williams, C. R., Ecklund, W. L., and Gage, K. S.: Classification of Precipitating Clouds in the Tropics Using 915-MHz Wind Profilers, J. Atmos. Ocean. Technol., 12, 996–1012, https://doi.org/10.1175/1520-0426(1995)012<0996:COPCIT>2.0.CO;2, 1995.

Williams, E., Rosenfeld, D., Madden, N., Gerlach, J., Gears, N., Atkinson, L., Dunnermann, N., Frostom, G., Antonio, M., Biazon, B., Camargo, R., Franca, H., Gomes, A. M., and Lima, M. A.: Contrasting convective regimes over the Amazon: Implications for cloud electrification., J. Geophys. Res., 107, 8082, https://doi.org/10.1029/2001JD000380, 2002.

Yuter, S. E. and Houze, R. A.: Three-dimensional kinematic and microphysical evolution of Florida cumulonimbus. Part II: Frequency distribution of vertical velocity, reflectivity, and differential reflectivity, Mon. Weather Rev., 123, 1941–1963, 1995.